A Novel Analytical Tool to Capture Wind Profile Variability for Wind Energy Assessment: Fast, Simple, and Beyond State-of-the-Art in Complex Terrain

Brandon J.A. van Schaik[1], Alice J. Baruzier[1], Clément Loyer[1], Hendrik Huwald[1,2], and Michael Lehning[1,2]

[1]École Polytechnique Fédérale de Lausanne, EPFL ALPOLE Valais/Wallis, Route des Ronquoz 86, 1950 Sion, Valais, Switzerland

[2]WSL Institute for Snow and Avalanche Research SLF, Flüelastrasse 11, 7260 Davos, Graubünden, Switzerland

Correspondence: Brandon J.A. van Schaik (brandon.vanschaik@epfl.ch)

Abstract. ~~Reliable wind energy assessment is often limited by~~ The standardized wind turbine power performance method is limited by its reliance on single-point wind measurements at nacelle height, as ~~commonly used~~ prescribed in international standards. Here, we present a closed-form analytical rotor-averaging model for turbine power that integrates the vertical variation of horizontal wind speed —- the changes in wind with height —- using a Taylor expansion of the inflow velocity over the rotor disk. We assess ~~idealised~~ idealized wind profiles to understand the isolated effects of typical shear, veer profiles, and turbulence on the power production of the turbine. This analytical model is then validated against power measurements from five Enercon E92 turbines on the Gotthard Pass, a complex-terrain wind park in the Swiss Alps, across 10 distinct wind events. The analytical model consistently outperforms both OpenFAST simulations and the International Electrotechnical Commission (IEC) standards, providing smoother and more accurate power estimates, reducing RMSE by ~~8.8%~~ 8.8 % and bias by ~~25.4%~~ 25.4 % relative to IEC-standard single-point extrapolations. This equates to an annual energy production estimate that is ~~23.7 *MWh*~~ 23.7 MWh closer to reality, for a ~~2.35 *MW*~~ 2.35 MW turbine at this ~~specific~~ complex terrain site. Additionally, it enables effective filtering of wake-affected LiDAR measurements, demonstrating flexibility, robustness, and applicability for pre-construction assessment and wind park expansion in complex terrain.

1 Introduction

~~Accurately modelling~~ Accurate modelling of wind turbine power generation requires more than ~~a simplistic application of the power curve~~ the direct application of hub-height power curves. Standard power curves, as defined in IEC 61400-12-1, rely on mean wind speed at hub height ~~. Traditional~~ and therefore fail to capture complex atmospheric conditions that significantly influence power production (IEC, 2022; Santos et al., 2015). Resulting uncertainties are closely linked to wind variability, turbulence, and boundary-layer processes, which remain insufficiently understood despite increasing turbine size (Belu and Koracin, 2012).

Although multi-height wind measurements from meteorological masts and Doppler-wind LiDAR are widely used and included in international standards, power performance assessments typically reduce the vertically varying inflow across the rotor-swept area to a single representative wind speed. This value is usually derived from a nacelle-mounted anemometer calibrated against the kinetic energy flux measured across the rotor plane approximately 2.5 rotor diameters upstream (IEC, 2022) . While appropriate for standardized test sites with flat or mildly complex terrain, this approach assumes quasi-uniform inflow across the rotor disk. In complex terrain, however, strong vertical and lateral ~~wind velocity gradients~~ gradients caused by wind shear, directional veer, turbulence, yaw misalignment, and wake effects violate this assumption, leading to increased uncertainty in power curve application.

Turbulence intensity strongly influences measured power curves, as standard 10-minute averaging obscures short-term variability and complicates comparisons with guaranteed performance (Albers, 2010). Wind shear and directional veer further modify the effective inflow, such that alignment with hub-height wind may lead to sub- or super-optimal power production depending on the vertical profile (Murphy et al., 2020). These effects are amplified in complex terrain, where non-homogeneous upstream flow alters wake development and induction compared to flat, homogeneous conditions (Troldborg et al., 2022; Gasser et al., 2026 . Despite these limitations, the reduction of spatially varying inflow to a single-point ~~standard for historical consistency in~~ wind speed remains the prevailing standard for consistency in power assessment (IEC, 2022).

In recent years, simulations and analytical approaches that explicitly account for spatial wind velocity distributions have gained attention for their ability to capture key ~~physical power~~ processes influencing turbine power output. Modified power curve and induction models incorporating wind shear, veer, turbulence intensity, and yaw misalignment improve power prediction accuracy by up to 51 % (Vahidzadeh and Markfort, 2019, 2020). Similarly, coupling actuator disk theory with blade-element models to resolve vertical shear and directional ~~improves correlation with observed~~ changes improves agreement with observed turbine power and reduces prediction errors (Mata et al., 2024). At the wind-farm scale, Gaussian process and random forest approaches further highlight the importance of accounting for wake-induced turbulence and vertical ~~wind profile~~ profile variability, showing good agreement with large-eddy simulations and observations (Niayifar and Porté-Agel, 2015; Clifton and Wagner, 2014).

~~.~~ Early power-performance studies showed that the sensitivity of measured power curves to atmospheric conditions partly reflects limitations in the reference wind-speed definition. Using multi-level measurements across the rotor layer, Elliott and Cadogan (1990 demonstrated that stratifying power curves by turbulence intensity yields substantially different outputs at identical hub-height wind speeds, largely due to systematic deviations between hub-height and disk-averaged wind speeds under low-turbulence, strongly sheared conditions. In such regimes, hub-height wind speed frequently overestimates disk-averaged velocity, indicating that single-point measurements can bias the inferred kinetic input and distort interpretations of power-curve scatter and apparent underperformance (Elliott and Cadogan, 1990).

~~of wind speed~~ Motivated by these findings, several studies proposed replacing hub-height wind speed with an equivalent or rotor-averaged wind speed that better represents rotor-integrated inflow. Simulation studies over flat terrain showed that electrical power correlates more strongly with Rotor Equivalent Wind Speed (REWS), derived from measurements across the swept area, than with hub-height wind speed, highlighting that identical hub-height values can correspond to substantially

different rotor-layer kinetic energy (Wagner et al., 2009). A widely adopted formulation defines REWS by matching the kinetic energy flux through the rotor, resulting in a cubic (energy-based) rotor-area weighting:

$$U_{eq} = \left(\sum_i u_i^3 \frac{A_i}{A} \right)^{1/3} \tag{1}$$

where u_i represents wind speed measurements associated with rotor-area segments. In LiDAR-based applications, this energy-equivalent definition reduces power-curve scatter and yields a power coefficient consistent with the profile-integrated kinetic energy flux, rather than the hub-height approximation (Wagner et al., 2011).

As rotor-equivalent wind-speed methods gained wider adoption, their practical implementation became an important topic. The IEA Wind Annex 32 comparative exercise showed that applying the IEC-draft REWS procedure requires explicit choices in assigning rotor-area weights to discrete measurement heights, including the definition of segment areas and the treatment of measurements not located at rotor-tip elevations. Even for identical wind profiles, small but systematic differences in REWS were found across institutions due solely to variations in the segmentation and weighting approach, highlighting that REWS is not only a concept but also a method affecting reproducibility. The same study further showed that REWS-based power curves can differ substantially from hub-height-based curves, particularly under strong shear and low turbulence conditions, where inflow non-uniformity is most pronounced (Wagner et al., 2014).

Beyond shear-only corrections, several studies proposed veer- and turbulence-aware rotor-equivalent formulations to better represent the wind component normal to the rotor plane and its variability. In industry practice, "veer-aware" equivalent wind speeds apply a cosine projection of directional differences across the rotor, effectively down-weighting misaligned inflow (Antoniou et al., 2013). Choukulkar et al. (2016) developed an equivalent wind speed that combines rotor-area weighting with wind-speed and direction variability, accounting for turbulence intensity, directional shear, and flow misalignment. Similarly, Redfern et al. (2019) introduced a momentum-based rotor-equivalent wind speed with a veer correction by projecting wind vectors onto the turbine axis.

Field measurements confirm that intra-rotor flow variability can lead to substantial deviations from standard power curves. Combinations of wind shear and directional veer can induce power changes ranging from -19 % to +34 % relative to the nominal curve at a given hub-height wind speed (Mata et al., 2024). Differences between hub-height wind speed and REWS can exceed 70 kW, corresponding to up to 5 % of rated power for a single turbine (Murphy et al., 2020). These discrepancies can propagate to the wind-farm scale and may lead to significant instantaneous and cumulative power prediction errors, although their aggregate effect depends on how errors vary across turbines.

Ground-based Doppler wind LiDAR enables retrieval of wind speed and direction profiles across the rotor-swept area, allowing equivalent wind speeds to be derived based on kinetic energy flux rather than single-point measurements (Wagner et al., 2011) . Although IEC 61400-12-1 ~~standard~~ acknowledges that non-uniform inflow~~vertical and horizontal —~~particularly shear and turbulence ~~within the rotor-swept area, can significantly~~ across the rotor can bias power performance measurements~~stops short of prescribing~~ , it does not prescribe analytical methods to account for these effects, ~~suggesting the use of~~ instead recommending

weighted average wind speeds (IEC, 2022). This highlights a gap for physics-based formulations that explicitly resolve spatial wind variability across the rotor plane.

refer to the combined influence The benefit of adopting REWS over hub-height wind speed is not universal, as both can differ by less than 1 % under homogeneous conditions with weak shear, implying limited added value in such cases. However, larger deviations occur in complex terrain and atypical shear regimes, supporting the view that REWS-based normalization is most relevant where strong, non-linear shear and veer are frequent conditions typical of mountainous wind parks and central to this study (Van Sark et al., 2019).

In this study, we address this gap by proposing an analytical formulation for wind turbine power generation that evaluates the power equation as an integral over the rotor-swept area, rather than relying on a single wind-speed input. This approach incorporates vertically varying wind profiles and captures the combined effects of wind shear, directional veer, turbulence intensity, and yaw misalignmentacross the rotor disk as , here referred to as the intra-rotor flow structure, which governs the effective kinetic energy flux intercepted by the turbine.

To assess the performance of our analytical integration evaluate the proposed analytical approach, we rely on use numerical simulations from OpenFAST, an open-source wind turbine simulation tool developed by NREL (Jonkman, 2013). OpenFAST model developed by National Laboratory of the Rockies (NRL), formerly known as National Renewable Energy Laboratory (NREL) (Jonkman, 2013), which resolves turbine dynamics under realistic, spatially and temporally varying wind inflow , effectively capturing the intrarotor flow structure we aim to represent analyticallyinflow and captures the intra-rotor flow structure considered here.

This study focusses specifically on a highly The analysis focuses on a complex wind park site located at the Gotthard pass, in the heart of the Swiss Alpsat 2106m Pass in the Swiss Alps, 2106 m above mean sea level (a.m.s.l.We make use of). SCADA data from the five Enercon E92 (2.35MW) wind turbines installed there, while modelling a virtual wind 2.35 MW) turbines are used alongside simulations of a comparable turbine with open-source blade geometry, that is similar to the Enercon E92.

High-resolution wind profiles are taken obtained from the Gotthard Transect Experiment (van Schaik et al., 2025b), which includes LiDAR profiles collected comprising LiDAR measurements at 10 sites along a transect crossing through the Gotthard Wind Park. These LiDAR measurements not only across the wind park. These profiles provide wind speedand direction, direction, and turbulence intensity at 10 m vertical resolution , but also Turbulence Intensity (TI), which can be compared with real-world turbine performance under several under a range of complex flow conditions measured throughout the observed during a 3-month summer campaign.

In this manuscript, we We present and evaluate an analytical formulation for wind turbine power generation based on integrating wind velocity variations over the rotor plane, with a focus emphasis on vertical shear and turbulenceeffects. Benchmarked by model results of the same wind profiles in OpenFAST , we explore the various sources of error that are eliminated by, or still present in this novel method and present the improved accuracy of predicting wind turbine power . By benchmarking against OpenFAST simulations using identical inflow conditions, we assess remaining error sources and demonstrate improved accuracy in power prediction from standard wind profile measurements.

2 Methodology

Consider the standard wind turbine power equation, derived from the rotor ~~disc model in equation~~disk model in Equation 2:

$$P(v,z) = \frac{1}{2} C_p(v) \rho A v(z)^3 \tag{2}$$

where ~~$P(v,z)\,[kW]$~~ $P(v,z)\,[\mathrm{kW}]$ is the power extracted by the turbine at wind speed ~~$v(z)\,[m\,s^{-1}]$~~, ~~$C_p(v)\,[-]$~~ $v(z)\,[\mathrm{m\,s^{-1}}]$, $C_p(v)\,[-]$ is the power coefficient, representing the efficiency of the turbine at converting kinetic energy into mechanical energy, ~~$\rho\,[kg\,m^{-3}]$~~ $\rho\,[\mathrm{kg\,m^{-3}}]$ is the air density which is assumed to be constant throughout the swept area of the blade~~,~~ ~~$A = \pi R^2\,[m^2]$~~. $A = \pi R^2\,[\mathrm{m^2}]$ is the rotor-swept area with R the rotor radius, and $v(z)^3$ reflects the cubic dependence of power on wind speed. In this formulation, wind speed is typically assumed to be uniform and measured at hub height.

However, in reality wind velocity varies vertically and horizontally due to atmospheric shear. Among these, vertical variations across the rotor-swept area are usually the dominant factor, often far exceeding horizontal deviations. This dominance of vertical variations is well established in boundary-layer meteorology (Stull, 1988) and wind energy practice (Wagner et al., 2014; IEC, 2022), where horizontal variations across the rotor disk are usually minor compared to the strong vertical gradient in wind speed, although this assumption may not hold in the presence of turbine wakes, which we only consider as an edge case here (Section 3.3).

2.1 Analytical ~~method~~model : Taylor series approximation

2.1.1 Model applied to non-turbulent wind profiles

To address these vertical variations in the horizontal wind speed, we integrate over the rotor-swept area along the z-axis by $\mathrm{d}z$ as shown in Figure 1.

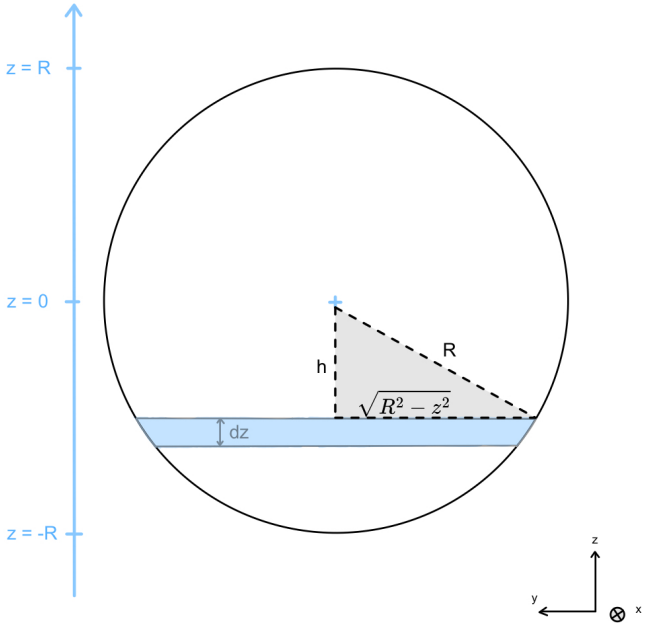


Figure 1. Vertical integration over the rotor-swept area of a wind turbine.

From which we find ~~equation~~Equation 3:

$$P(v) = \frac{1}{2} C_p(v) \rho \int_{-R}^{R} 2\sqrt{R^2 - z^2}\, v(z)^3 dz \quad (3)$$

Where ~~$R\,[m]$~~ R [m] is the radius of the rotor-swept area of the turbine, and $z\,[m]$ is the vertical variable. $z = 0$ is defined at the nacelle of the turbine, and $-R$ and R and the bottom and top of the swept area of the blade. Here, one can integrate over any vertical wind speed function; however due to the cubic relation with wind power, this integral often has no analytical solutions.

Since the vertical wind profile is continuous and differentiable across the whole rotor-swept area, one can expand the wind profile into its Taylor series of order N:

$$v(z) = \sum_{i=0}^{N} c_i z^i = c_0 + c_1 z + c_2 z^2 + ... + c_N z^N \quad (4)$$

Expanding the vertical wind profile into a Taylor series is a flexible method for representing wind speed across the rotor-swept area. In practice, wind measurements are often available at varying and non-standardized heights, depending on the instrumentation and site conditions, while turbine hub heights and rotor diameters also differ substantially. The Taylor expansion allows incorporation of such heterogeneous data in a single algorithm, as it can approximate the wind profile locally using information from any set of measurement heights. Moreover, since the wind profile is assumed to be continuous and differentiable, a

low-order Taylor polynomial (we recommend $N = 3$) is typically sufficient to capture the essential vertical shear characteristics while avoiding overfitting to noise in the data. This provides a good balance between accuracy and simplicity.

By inserting the series expansion of Equation 4 into the integrand of Equation 3, the integral can be solved analytically for any wind profile $v(z)$. The full derivation is given in Appendix A, with the resulting expression shown in Equation 5:

$$P(v) = \frac{1}{2} C_p(v) \rho A \sum_{i,j,k=0}^{N} c_i c_j c_k R^m \frac{m!}{2^m (\frac{m}{2}!)^2 (\frac{m}{2}+1)} K_m, \quad m = i+j+k \,|\, m \text{ is even} \tag{5}$$

Where ~~the~~ we separate the large fractional term of factorials, $K_m[-]$ for readability:

$$K_m = \frac{m!}{2^m (\frac{m}{2}!)^2 (\frac{m}{2}+1)}, \quad m = i+j+k \,|\, m \text{ is even} \tag{6}$$

In Equation 5, the summation refers to a triple summation over all Taylor expansion coefficients i, j~~&~~, and k. This is particularly useful to assign an approximate, but continuous function to the discrete wind profile measurements, such that the following derivation can be treated analytically. The fractional term with ~~m~~ K_m is the reciprocal factor resulting from an integration of a variable raised to an exponent shown in Table ~~??~~A1. Crucially, this factor is set to 0 for uneven values of m. The summation is terminated by N, which can be increased ~~arbitrarly~~ arbitrarily to converge the Taylor series as close to the original function $v(z)$ as desired, but will result in several higher-order terms, which exponentially decrease in contribution to the power production of the wind turbine.

~~Lookup table of the fractional term in equation 5. m fraction 0 1 2 $\frac{1}{4}$ 4 $\frac{1}{8}$ 6 $\frac{5}{64}$ 8 $\frac{7}{128}$ 10 $\frac{21}{512}$~~

To facilitate the use and reproducibility of the method presented here, we provide an open-source workflow that automates the two steps of solving for ~~equation 4 &~~ Equation 4 and 5: a) given arrays of measured 10 min mean wind speeds v and heights z, the code fits a Taylor polynomial of user-selected order N (recommended at $N = 3$ providing a good trade-off between capturing essential behaviour and avoiding over-fitting), and b) evaluates ~~equation~~ Equation 5 exactly by performing the triple summation, applying the fraction terms in Table~~??~~ A1, and returning the total power $P(v)$ together with per-order contributions of m. The code accepts R, ρ, and a tabulated $C_p(v)$ curve that sufficiently covers the working wind speed range of any wind turbine. The $C_p(v)$ tabulated data is selected by the spatial average of the wind speed across the swept area of the blade, as to represent the coefficient of performance most accurately to any arbitrary wind profile. The archived, citable release containing these scripts and an example of the Enercon E92 wind turbines, used in this study, are available on Zenodo (van Schaik et al., 2025a). We refer the reader to the Data Availability ~~section~~ Section of this manuscript for more details.

2.1.2 ~~Turbulence~~Model applied to turbulent wind profiles

For the case of turbulence, we must briefly depart from the formulations above and instead focus only on the second-order statistics of wind speed fluctuations. While measurements from ~~van Schaik et al. (2025)~~ van Schaik et al. (2025b) show that a Student-t distribution provides the most accurate fit, we assume a normal distribution with mean ~~$\overline{v}$~~ $\overline{v}\,[\mathrm{m\,s^{-1}}]$ and standard deviation ~~$\sigma_{\overline{v}}$~~ $\sigma_v\,[\mathrm{m\,s^{-1}}]$, as it is the only second-order distribution that allows for analytical treatment, while still offering a

sufficiently satisfying fit of the randomness of turbulence. It has been shown that a linear scaling factor of ~~1.81~~ 1.81 applied to σ_v effectively accounts for the heavier tails of the Student-t distribution in the case of the Gotthard Transect Experiment for all wind directions and speeds (van Schaik et al., 2025b). Therefore, the estimated probability density function describing the turbulence is assumed to be:

$$f(v) = \frac{1}{\sqrt{2\pi\sigma_v^2}} \exp\left(-\frac{(v-\overline{v})^2}{2\sigma_v^2}\right) \tag{7}$$

To realistically estimate the impact of turbulence on power production, the expected power output in the presence of turbulence must be obtained by integrating the full turbine power curve $P(v)$ (~~eq.~~ Equation 2) over the probability distribution of wind speeds:

$$\Delta P_{\text{turb}}(\overline{v}, \sigma_v) = \int_{v_{\text{in}}}^{v_{\text{out}}} P_{pc}(v) f(v)\, dv\mathrm{d}v \tag{8}$$

Where $\Delta P_{\text{turb}}(\overline{v}, \sigma_v)\,[kW]$ gives us the contribution of turbulence which is positive in the convex part of the power curve, and negative in the concave part of the power curve. ~~To assess its validity, we compared the turbulence contribution against theoretical wind profiles with constant height in OpenFAST, showing good agreement with the analytical solution (Fig. 7b, further detailed in the Results)~~$P_{pc}(v)\,[kW]$ is an analytical estimate of the power curve (Equation 9), and $v_{\text{in}}\,[m\,s^{-1}]$ and $v_{\text{out}}\,[m\,s^{-1}]$ denote the cut-in and cut-out wind speeds.

Here, we propose to use the following analytical approximation of the turbine power curve ~~$P(v)$~~ $P_{pc}(v)$, which fits well both the Enercon E92 of the Gotthard pass measurement campaign of this study and many other commercial wind turbines ~~well~~ used around the globe (van Schaik et al., 2026; van Schaik et al., 2026):

$$P_{pc}(v) \approx P_r 1 - \exp - \frac{v - v_{in}}{B} C \approx \begin{cases} 0, & v \le v_{in} \\ P_r\left(1 - \exp\left[-\left(\frac{v-v_{in}}{B}\right)^C\right]\right), & v_{in} < v \le v_{out} \\ 0, & v > v_{out} \end{cases} \tag{9}$$

This formulation captures the rapid increase in power after cut-in (v_{in}), and the saturation near rated power ~~. Parameters B and C~~ $P_r\,[\text{kW}]$. Parameters $B\,[\text{m s}^{-1}]$ and $C\,[-]$ can be adjusted to fit the performance of a specific turbine.

Having established a general framework for turbulence inclusion in an analytical fashion, we can now return to ~~equation~~Equation 8 and extend it to account for ~~vertical~~ variations in the wind speed gradients across the rotor-swept area – which represents turbulence – by calculating the correction term. This method and code is also archived on Zenodo as a citable release of scripts along with example data of the Enercon E92 turbines including wind and turbulence profiles from the Doppler wind LiDAR of the Gotthard Transect Experiment (van Schaik et al., 2025a).

2.1.3 ~~Wake filtering~~Power fitting

~~Another useful feature of~~ The analytical formulation of Equation 9 is fitted to the published power curve of the ~~Taylor-expanded wind profile is that it naturally enables the removal of anomalous or clearly unphysical measurements before constructing the analytical profile. Because our method relies only on a small number of vertically adjacent points, any range gates that contain erroneous values, such as flow disturbances caused by upstream turbine wakes, can simply be discarded with few consequences for the overall reconstruction of the wind profile. This approach is appropriate either when the objective is to recover the undisturbed wind profile, or when the LiDAR happens to sit inside a wake while the turbine location of interest lies just outside of it. The Taylor expansion is then fitted to the remaining clean measurements immediately above and below the wake region, yielding an interpolated representation of the approximated undisturbed wind field.~~

~~The same filtering approach extends directly to the turbulence statistics. Wakes typically manifest as abrupt increases in the standard deviation of the horizontal wind , σ_v. These range gates can be removed in the same manner as for~~ Enercon E92 2.35 MW wind turbine using manufacturer data from the technical specifications. The fit parameters are determined as $v_{in} = 1\,\mathrm{ms}^{-1}$, $P_r = 2350\,\mathrm{kW}$, $B = 8.16\,\mathrm{ms}^{-1}$, and $C = 3.68$, with the ~~mean wind speed to create a wake-free estimate of the turbulence structure. These Taylor expansion parameters of the mean wind and turbulence profile then serve as the input to Equation 5 as discussed above.~~ cut-out wind speed implicitly represented at $v_{out} \approx 25\,\mathrm{ms}^{-1}$. As shown in Figure 2, the proposed analytical function reproduces the key characteristics of the turbine power curve with excellent agreement, achieving a coefficient of determination of $R^2 = 0.9996$. In particular, the rapid increase in power after cut-in and the smooth transition toward the rated power plateau are well captured by the exponential term inspired by a Weibull Cumulative Distribution Function (van Schaik et al., 2026).

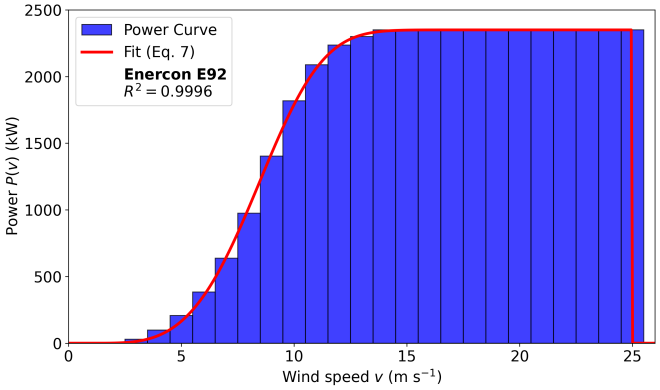


Figure 2. Fitting of Equation 9 to the Enercon E92 2.35 MW turbine.

2.2 ~~Numerical method~~

This strong agreement demonstrates that the proposed functional form is sufficiently flexible to accurately represent real turbine behaviour while remaining analytically computable. Although the fit is shown here for the Enercon E92, similar performance has been observed for a wide range of commercial wind turbines, making this formulation broadly applicable from small kilo-Watt scale to large mega-Watt scale turbines (van Schaik et al., 2026). The resulting closed-form expression of the power curve is especially advantageous for subsequent analytical developments, as it enables direct integration and incorporation into turbulence-resolving formulations without relying on discrete lookup tables or numerical interpolation.

2.2 Numerical model: OpenFAST simulations

Having established the analytical method in the previous section, we now move to a state-of-the-art numerical method of simulating wind power produced by wind turbines based on a vertical wind profile. For this method, we make use of the Open source wind turbine simulation software OpenFAST.

2.2.1 Introduction to OpenFAST

To validate the developed equations, we make use of OpenFAST coupled with TurbSim to simulate any inflow wind profilesapplied to a single wind turbine. OpenFAST is a multi-physics simulation tool developed by ~~the National Renewable Energy Laboratory (NREL~~ NREL (NRL as of 1 December 2025) in the United States (Jonkman, 2013) ~~. In~~ which includes TurbSim, a turbulent-wind simulator.

Previous studies have demonstrated that OpenFAST is a highly accurate tool for generating realistic turbulent wind fields, particularly through the stochastic modelling capabilities of its TurbSim module. In particular, the work of Brown et al. (2024) validated the performance of OpenFAST by comparing turbulent simulations against 253 ten-minute bins of turbine measurement data collected during normal operation. Their results showed strong agreement in both power performance and structural

load predictions. Beyond its validated accuracy, OpenFAST has also been widely adopted as a reference framework for advanced wind energy modelling and simulation in turbulent conditions. As described by Sprague et al. (2020), OpenFAST constitutes the core aeroelastic solver within their ExaWind multi-fidelity modelling framework, enabling coupling with turbulence-resolving flow solvers such as large-eddy simulations as well as lower-fidelity inflow models. This modular and physics-based architecture makes OpenFAST particularly well suited as a baseline for the validation of our analytical model in the context of turbulent flows in complex terrain.

TurbSim is a stochastic turbulence simulator primarily designed for use within the InflowWind module. In this study, ~~the~~ TurbSim is not only used to generate turbulent wind fields but also to define user-defined wind profiles via the WindProfileType option, thus enabling realistic wind input with vertical variations.

2.2.2 Common simulation parameters

In this study, the following OpenFAST modules were activated: InflowWind, ElastoDyn, AeroDyn, and ServoDyn. All settings were kept at their default values, with two exceptions.

Firstly, the shaft tilt angle was set to $0°$ (instead of the default $5°$) in order to remain consistent with the analytical method, which assumes a purely horizontal inflow and ~~maximises~~ maximizes power capture under that condition. Although the Enercon E92 turbine – which is used extensively in this study – is built with a shaft tilt, this simplification is acceptable because our final comparison is between the analytical model and the OpenFAST model, for which the associated errors largely cancel out. ~~When comparing to the measured power output of the turbine (P_{true}), setting the shaft tilt to zero introduces a small bias of approximately $8\,kW$ for the $2.35\,MW$ turbine. However, since the wind profile is based on a LiDAR measurement located roughly $100\,m$ from the turbine, any slight decrease in horizontal inflow or the inclusion of vertical wind components caused by shaft tilt would not significantly improve the accuracy. Therefore, we chose to retain the simpler configuration which are comparable to the idealised wind profiles.~~

Secondly, the degrees of freedom associated with tower deformation were disabled to focus the analysis on wind effects and power production, excluding the influence of structural flexibility.

~~TurbSim is a stochastic turbulence simulator primarily designed for use within the InflowWind module. In this study, TurbSim is not only used to generate turbulent wind fields but also to input user-defined wind profiles via the WindProfileType option. These files are~~ The turbulence and wind profile parameters are generated using TurbSim whose output file is then read by the InflowWind module ~~to provide the wind data necessary for the OpenFAST simulation, thus enabling realistic wind input with vertical variations~~of OpenFAST and provide the necessary wind data for the simulation.

To ensure a reproducible approach, the wind turbine model selected is part of a reference series developed by the NREL to serve as standard benchmarks. This series is known as WindPACT, and we use the 3.0 MW NREL WindPACT turbine for our numerical studies, as it is the closest open-source representation of the Enercon E92 turbines deployed on the Gotthard pass. The exact specifications of both turbines can be found in Table 1. While the NREL ~~3.0 MW~~ 3.0 MW WindPACT turbine differs from the Enercon E92 2.35 MW in terms of rated power, rotor diameter, and specific blade geometry, it represents the closest openly available model for numerical simulations in OpenFAST. We cannot directly use the Enercon E92 as its blade

geometries and aerodynamic specifications are proprietary. Any discrepancies in rated power or rotor characteristics between the two turbines must be accounted for ~~in the following methodology~~and their consequent errors are discussed in the Results and Discussion Section 3.4.

Table 1. Specifications of the Enercon E92 and NREL WindPACT turbines.

Turbine	Enercon E92	NREL WindPACT
Location	Gotthard pass	OpenFAST
Blade diameter [m]	~~92 m~~ 92	~~100 m~~ 100
Nacelle height [m]	~~98 m~~ 98	~~119 m~~ 119
Rated power [kW]	~~2.35 MW~~ 2350	~~3.0 MW~~ 3000
Rated wind speed [$\mathrm{m\,s^{-1}}$]	~~14 ms^{-1}~~ 14	~~12 ms^{-1}~~ 12
Cut-in wind speed [$\mathrm{m\,s^{-1}}$]	~~2 ms^{-1}~~ 2	~~1 ms^{-1}~~ 1
Cut-out wind speed [$\mathrm{m\,s^{-1}}$]	~~25 ms^{-1}~~ 25	~~NONE~~ None
Air density [$\mathrm{kg\,m^{-3}}$]	~~0.996 kgm^{-3}~~ 0.996	~~0.996 kgm^{-3}~~ 0.996

~~Each simulation runs~~ The simulations are run for 12 minutes of turbine operation under steady wind conditions, meaning that both the mean wind speed and the turbulence intensity are held constant throughout the simulated period. During the first 2 minutes, the turbine adjusts from its initial power setting of ~~3.0 MW~~ 3.0 MW to the stable operation power. To avoid including this adjustment period, the average power output is calculated over the final 10 minutes. Power curves are generated for wind speeds ranging from ~~1 ms^{-1} to 25 ms^{-1}~~ 1 to 25 in increments of ~~1 ms^{-1}~~ 1, resulting in 25 simulations per power curve.

2.3 ~~Idealised wind profiles~~

~~To compare the influence of specific parameters, the difference in power output $\Delta P_{\text{parameter}}$ $[kW]$ between the reference and the modified configurations is evaluated using the following expression~~

2.2.1 Differences in Power Curves

As mentioned previously, we have aligned our simulations with the Enercon E92 2.35 MW wind turbines installed at the Gotthard Wind Park. Power curve data is taken from the Enercon E92 specification sheet and is fitted (Equation 9), resulting in a smooth analytical expression (Figure 3a).

Remaining with Figure 3, the OpenFAST simulations cannot be based on the Enercon E92 directly, as the required blade geometry to simulate power production is proprietary. Instead, the open-source WindPACT 3.0 MW turbine is used. This has consequences in all upcoming results since the turbine behaves differently due to the small variations in the shape of the power curves. For example, the WindPACT turbine's $C_p(v)$ exhibits unrealistic features starting at extremely high values after which it remains unrealistically constant until the rated power is reached. Furthermore, the turbine power curve lacks defined cut-in and cut-out wind speeds, causing the model to produce power under wind conditions where a real turbine would not operate. This likely leads to an overestimation of energy production, particularly during very low and very high wind events.

Crucially, there is a difference in how these two power curves were derived; the Enercon E92 power curve results from long-term measurements which average over a large number of real wind profiles. This is strictly different form the WindPACT wind profile which is based on a uniform wind profile where v is constant with height, i.e. the reference case mentioned in

Section 2.3. In reality, the uniform wind profile assumption could be better represented by a logarithmic or power-law wind profile that more closely represents the wind profiles incident on the Enercon E92. However, this introduces an additional shear parameter (i.e. z_0 or α) that we can not accurately define as the wind profile information regarding the Enercon E92 power curve calibration was not reported. One could attempt to estimate this value knowing the test site topography, but uncertainties would remain as this shear parameter is largely influenced by atmospheric stability and wind direction (Bot, 2016; Emeis, 2005).

Furthermore, the IEC 61400-12-1:2022 standard outlines that the power curve calibration – as performed for the Enercon E92 – requires the use of a nacelle-mounted LiDAR which performs a cubic-weighted average of the incoming wind field at nacelle height (IEC, 2022; Wagner et al., 2011). Considering that commercially available nacelle-mounted LiDARs tend to scan in a cone pattern, wind speed values from the entire swept area of the blade will be included in this averaging (Letizia et al., 2023; Rettenmeier et al., 2013). According to the standard, the nacelle-mounted anemometer shall be calibrated to this spatially cubic-weighted average wind speed. This would indeed convert the realistic, non-uniform wind profile into a single wind speed value, which can be treated as constant throughout the whole swept area of the wind turbine; in other words, a uniform flow profile.

$$\Delta P_{\text{parameter}} = P_{\text{parameter}} - P_{\text{ref}}$$

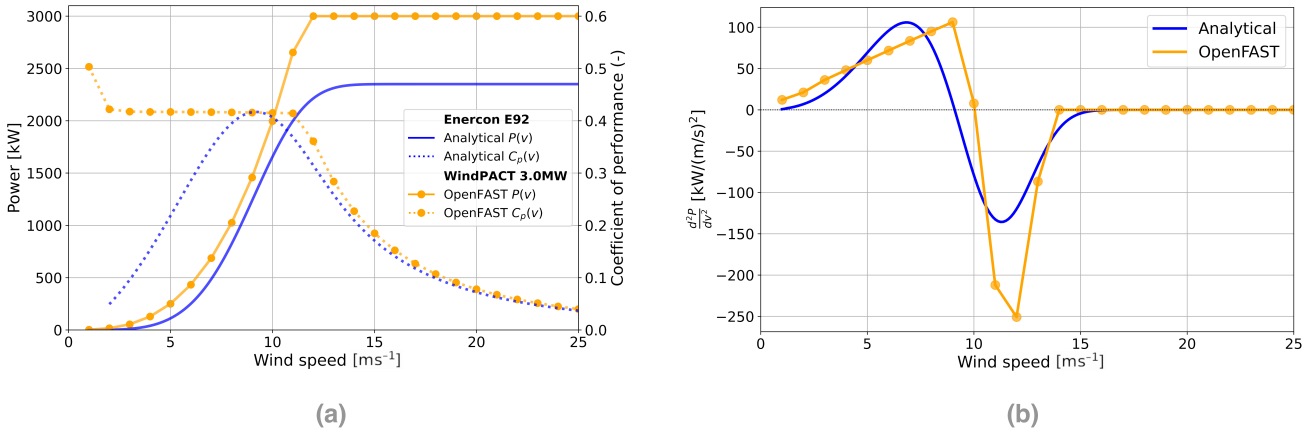


Figure 3. Comparison of the Enercon E92 2.35 MW and WindPACT 3.0 MW power curve, coefficient of performance and curvature. (a) Power curves $P(v)$ and coefficients of performance $C_p(v)$, and (b) Curvature of the power curves.

~~where $P_{\text{parameter}}\,[kW]$ is the power output with the parameter under study, and $P_{\text{ref}}\,[kW]$ is the power output from the reference case. The reference case corresponds to an horizontal, constant and uniform wind profile with no turbulence, which is detailed in section 3.1.~~ The power curve's second derivative, representing the curvature, is shown in Figure 3b. This curvature is physically relevant, since it is directly responsible for the power production response on vertical wind speed variations across the swept area of the turbine. When parts of the turbine blade sweeps through different wind speed regimes, this curvature controls the degree to which these variations translate to power production. Notice the smooth curvature of the analytical Enercon E92 power curve, while the WindPACT 3.0 MW turbine exhibits a linear increase before an abrupt drop. The same features of linear power discrepancies and abrupt changes are observed throughout the following results.

2.3 Methodology for Idealized Wind Profiles

2.3.1 Idealized Profiles based on Wind Characteristics

We preface the more complex simulations from the Gotthard Transect Experiment with several ~~idealised~~ idealized profiles to understand the effects of individual wind profile phenomena.

To compare the influence of those flow characteristics, the difference in power output $\Delta P_{\text{parameter}}\,[\text{kW}]$ between the reference and the modified configurations is evaluated using the following expression:

$$\Delta P_{\text{parameter}} = P_{\text{parameter}} - P_{\text{ref}} \tag{10}$$

where $P_{\text{parameter}}$ [kW] is the power output with the parameter under study, and P_{ref} [kW] is the power output from the reference case.

In this study, we will cover the following ~~idealised~~ idealized wind profiles:

a) Uniform profile (reference case): is the most simplistic case where $\frac{dv}{dz} = 0$, i.e. the wind speed is not a function of height. This is used as the reference case for comparing to the standard power curve model in the IEC standard, defined by ~~equation~~ Equation 2. In our study, we likewise adopt this uniform profile as the ~~base~~ reference case, against which the subsequent ~~idealised~~ idealized wind profile scenarios are compared.

b) Linear shear: $v(z) = az + \overline{v}$ (~~Fig.~~Figure 4a). Where ~~,~~ the analytical power production can be derived by ~~equation~~ Equation 11:

$$\Delta P_{\text{shear, an}} = \frac{3}{4} \cdot \frac{R^2 a^2}{\overline{v}^2} \cdot P_{\text{ref}} \tag{11}$$

Where the subscript an refers to the analytical solution derived from the integral ~~Eq. 3, $a = 0.01/0.025/0.05\,[s^{-1}]$~~ Equation 3, $a = 0.01/0.025/0.05\,[\text{s}^{-1}]$ is the shear coefficient, and ~~$z = 0\,m$~~ $z = 0$ is defined at the nacelle of the turbine, ~~and~~ with $-R$ and R and the bottom and top of the swept area of the blade, respectively. Figure 4a illustrates the shear parameter across the rotor area.

c) Linear veer: where $\frac{d\theta}{dz} = \alpha = \text{const.}$, such that the wind profile is defined as $v(z) = \overline{v} cos(\alpha z)$ (~~Fig.~~Figure 4c). Such that, the analytical power production is given by ~~equation~~ Equation 12:

$$\Delta P_{\text{veer, an}} = -\frac{3}{8} \cdot \alpha_{\text{max}}^2 \cdot P_{\text{ref}} \tag{12}$$

where ~~$\alpha_{\text{max}} = \alpha R = 5/10/22.5\,[°]$~~ $\alpha_{\text{max}} = \alpha R = 5/10/22.5\,[°]$ is the maximum angular deviation at the upper and lower extents of the rotor-swept area. Figure 4c shows the definition of this veer parameter.

d) Vertically-constant TI: in which the Turbulence intensity is defined as ~~$TI = \frac{\sigma_v}{\overline{v}}$~~ TI $= \frac{\sigma_v}{\overline{v}}$, and it is constant with height ~~$\frac{dTI}{dz} = 0$~~ $\frac{d\text{TI}}{dz} = 0$. Here, the analytical power production can not be expressed analytically in closed form, but is best represented in integral form (~~eq.~~ Equation 8). In which, the turbulence intensity is governed in TurbSim by the parameter "IECturbc", where the user can simply enter ~~TI $= 10/15/20/25\%$~~ TI $= [10, 15, 20, 25\,\%]$.

e) Logarithmic wind profile: is a typical wind profile used in a plethora of boundary-layer studies, defined by a logarithmic relation between wind speed and height: ~~$v(z) = \frac{u^*}{\kappa} ln\left(\frac{z}{z_0}\right)$~~ (~~Fig.~~$v(z) = \frac{u_*}{\kappa} ln\left(\frac{z}{z_0}\right)$ (Figure 4b). Where ~~$u^*\,[m\,s^{-1}]$~~ $u_*\,[\text{m}\,\text{s}^{-1}]$ is the friction velocity, ~~$\kappa \approx 0.41$~~ $\kappa \approx 0.41\,[-]$, is the Von ~~Kárman~~ Kármán constant, and ~~$z_0 = 0.1\,[m]$~~ $z_0 = 0.1\,[\text{m}]$ is the surface roughness, which was chosen based on logarithmic fits of the wind profiles measured by the LiDAR on the Gotthard pass. It is the most realistic theoretical wind profile of wind over a surface. From this, the power curve can be calculated by ~~equation~~ Equation 5, with no closed-form solution.

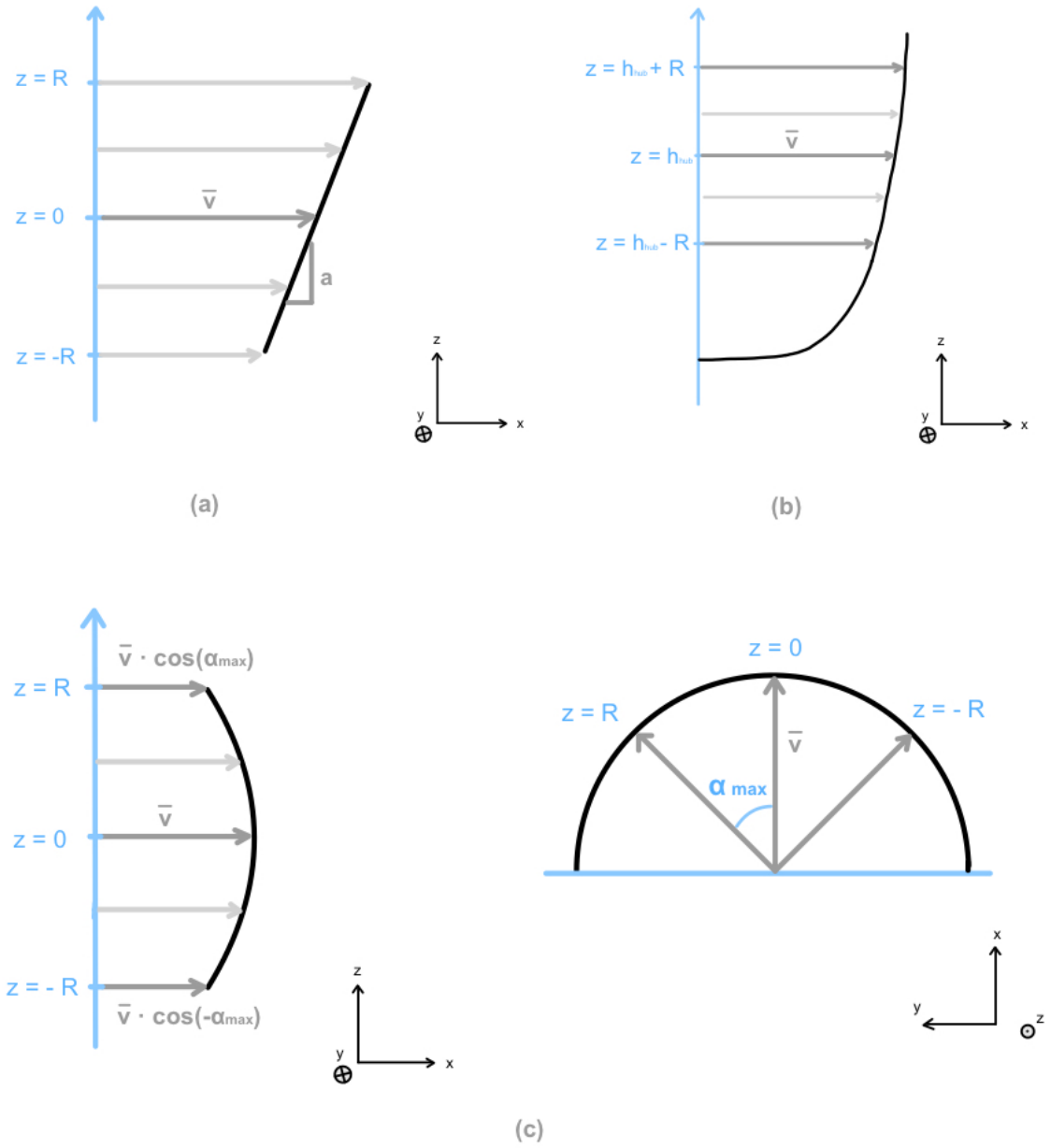


Figure 4. ~~Idealised~~ Idealized vertical wind profiles used in controlled simulations: (a) linear shear, (b) ~~Logarithmic~~ logarithmic wind profile, and (c) linear veer.

2.4 ~~Measured wind profiles~~

~~Wind power~~

2.3.1 Validation

Based on these different types of idealized vertical wind profiles, we compare the analytical and numerical deviations from the reference case in Results and Discussion Section 3.1, where we discuss differences that may arise from the differing power curves used in the methods, as well as other systematic differences between the models.

2.4 Methodology for the Gotthard-measured wind profiles

With the understanding of the individual contributions and effects of the different models used to estimate wind turbine power from the vertical wind profiles, we move to a real-world complex terrain example on the Gotthard pass, in the Swiss Alps. In this subsection, we outline the wind profiles that were measured in a Doppler-wind LiDAR campaign, and detail the processing steps required to compare the novel analytical model to the state-of-the-art numerical model.

2.4.1 The Gotthard Campaign

Real-conditions wind power output and nacelle wind speed data at 10-minute resolution were extracted from van Schaik et al. (2025b) for each of the five Enercon E92 wind turbines located at the Gotthard Wind Park. This wind farm is situated 2106 m ~~above mean sea level (~~a.m.s.l.~~)~~, north–south-oriented Gotthard Pass in the central Swiss Alps. The surrounding terrain is highly complex and ~~characterised~~ characterized by strong topographic channelling of the prevailing northerly and southerly winds. Linear shear and veer are consistently observed across all turbine sites, caused by upwind obstacles such as indicated orange in Figure 5a, and are known to impact rotor performance. Notably, the individual output of two turbines on the pass is approximately half that of each of the other three turbines, a disparity that cannot be explained by differences in mean wind speed alone.

In June to September 2023, the site hosted a Doppler wind LiDAR (VAISALA WindCube v2.1) campaign in which the instrument was deployed at 10 locations near the turbines over ~~a~~ the three-month period (Figure 5). This resulted in detailed wind profile measurements capturing both prevailing wind directions at each turbine site. The LiDAR retrieved three-dimensional wind velocity vectors at ~~10 m~~ 10 m vertical resolution between ~~40 m and 160 m~~ 40 m and 160 m above the instrument, and at ~~20 m resolution from 160 m to 300 m~~20 m resolution from 160 m to 300 m. Given the Enercon E92 nacelle height of ~~98 m~~ 98 m and rotor diameter of ~~92 m~~92 m, this setup provided 6 to 9 discrete wind speed and turbulence intensity measurements at ~~10 m~~ 10 m increments within the rotor-swept area, depending on the LiDAR location.

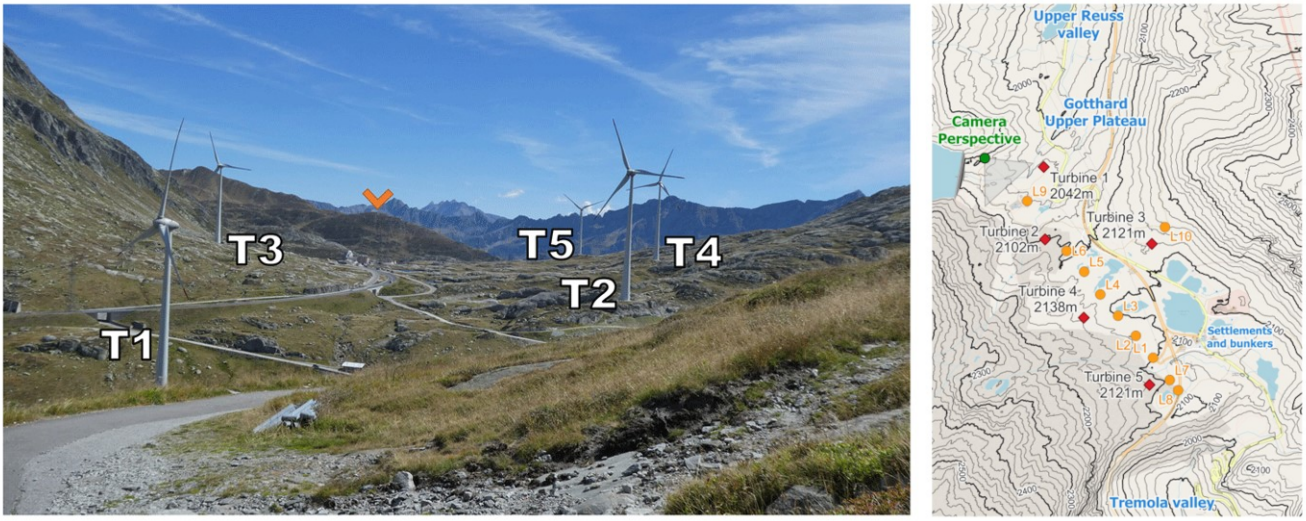


Figure 5. Turbine and LiDAR locations from the Gotthard Doppler wind LiDAR campaign in the Summer of 2023, from van Schaik et al. (2025b) ~~Fig.~~ Figure 2 and 3.

2.5 ~~Gotthard wind data: Analytical and simulation workflow~~

2.4.1 Numerical Model Workflow adapted to real wind profiles

The Doppler wind LiDAR profiles were also used to investigate the impact of vertical variations in incident wind speed ($v(z)$), and turbulence ($\sigma_v(z)$ measured by the LiDAR) in the rotor-swept area. Each measured wind profile is interpolated using a polynomial approximation (~~Eq.~~ Equation 4), of the order $N = 3$, and inserted into our analytical framework (Sec. 2.1), to compute expected turbine power output.

To compare these results to the state-of-the-art numerical method, the same LiDAR profiles are used as input for OpenFAST simulations whose results are then compared to the actual power production of the five Enercon E92 turbines. For each of them, a near-by and upwind LiDAR deployment location is selected based on the two prevailing wind directions: ~~Northerly~~ northerly and southerly. For each of the ten cases, we define a four-hour time window (subject to data availability) from which the corresponding LiDAR profiles are extracted for the simulations. Since the OpenFAST simulations are run on the NREL's reference WindPACT ~~3.0 *MW*~~ 3.0 MW turbine whose dimensions differ from the Enercon E92, a rescaling of the LiDAR profiles is performed. This transformation is a simple linear mapping, which scales the profiles to account for the height difference between the turbines, and includes any variation of altitude between the base of the Enercon E92 and its respective LiDAR deployment location. The heights of the LiDAR profiles are rescaled with Equation 13:

$$z_{new} = \frac{50}{46}(z_{old} + \Delta z_{lidar}) + 12.478 \tag{13}$$

where ~~$z_{new}\,[m]$~~ $z_{new}\,[\mathrm{m}]$ is the rescaled height point, ~~$z_{old}\,[m]$~~ $z_{old}\,[\mathrm{m}]$ the original height point, ~~$\Delta z_{lidar}\,[m]$~~ $\Delta z_{lidar}\,[\mathrm{m}]$ the altitude difference between the lidar and the turbine's base. The first factor results from the blade length of the WindPACT ~~3.0 MW ($R_{WP3.0} = 50\,m$~~3.0 MW ($R_{WP3.0} = 50\,[\mathrm{m}]$) versus the Enercon E92's (~~$R_{E92} = 46\,m$~~$R_{E92} = 46\,[\mathrm{m}]$). The additional constant ~~12.478 m~~ $12.478\,[\mathrm{m}]$ is simply a fit constant.

This scaling only affects the height values in the profiles; all the other variables are directly derived from the raw data of the LiDAR, which includes the velocity $v(z)$ and the wind speed dispersion $\sigma_v(z)$. Each transformed profile is then used as input for the TurbSim module prior to running the OpenFAST simulation. Regarding turbulence, two cases are considered when setting up TurbSim: ~~Firstly, for~~

- For simulations discarding turbulence, the turbulence model of TurbSim is set to *IECKAI* and the *IECturbc* parameter is set to 0 inside the ~~`TurbSim.inp`~~ `TurbSim.inp` file. This setup enables the definition of a custom wind profile inside the ~~`TurbSim_User.profiles`~~ `TurbSim_User.profiles` while ensuring that the turbulence intensity is set to ~~0%.~~

  ~~Secondly, for~~ 0%.

- For simulations including turbulence, the Turbulence Model is set to *USRVKM*. This model discards the *IECturbc* parameter and enables user-defined *standard deviation* and *length scale* profiles to be defined in the ~~`TurbSim_User.profiles`~~ `TurbSim_User.profiles` in addition to the velocity profile.

The standard deviation ~~$\sigma_v(z)\,[m/s]$~~ $\sigma_v(z)$ values are derived directly from the wind speed variability measured by the LiDAR. The length scale profile defines the size of the energy-containing eddies that cross the swept area with respect to the height. They are used by TurbSim to compute whether the eddies have a constructive or destructive effect on the transfer of wind power over the swept area. Since length scales were not part of the LiDAR measurements, the profile is set to the standard values of TurbSim as ~~$l = [3,4,6,9,13,13,13,...]\,[m]$~~ $l = [3,4,6,9,13,13,13,...]\,[\mathrm{m}]$.

The *USRVKM* model also takes into account standard eddies scales along the $(\boldsymbol{u}, \boldsymbol{v}, \boldsymbol{w})$ axes – $\boldsymbol{u}$ oriented along the wind flow, $\boldsymbol{v}$ vertical. These scales define the aspect ratio of the eddies globally; if all scales are identical, the eddies are considered spherical by TurbSim. Again, since this parameter is not part of the LiDAR measurements, the scales are set to default for the simulations, that is, ~~(1.092, 1.0, 0.534)~~(1.092, 1.000, 0.534).

The TurbSim module then computes a binary file ~~`TurbSim.bts`~~ `TurbSim.bts` which is called by the OpenFAST input file ~~`InflowWind.dat`~~ `InflowWind.dat` when starting the simulation. Similarly to ~~2.2~~the settings presented in 2.2.2, the simulation is then run over 12min, and only the last 10min are considered in the final power output. Before comparing to the real power production of the Gotthard turbines, this output is scaled down by a factor ~~$k = \frac{2.35\,MW}{3.0\,MW}$~~ $k = \frac{2.35}{3.0}$ to account for the difference of rated power of the WindPACT turbine (~~3.0 MW~~3.0 MW) used in the simulation and of the Enercon E92 (~~2.35 MW~~2.35 MW) installed at the Gotthard.

In summary, the complete workflow of measured data variables, and how they are used in the analytical and OpenFAST simulations, is outlined in the schematic in Figure 6.

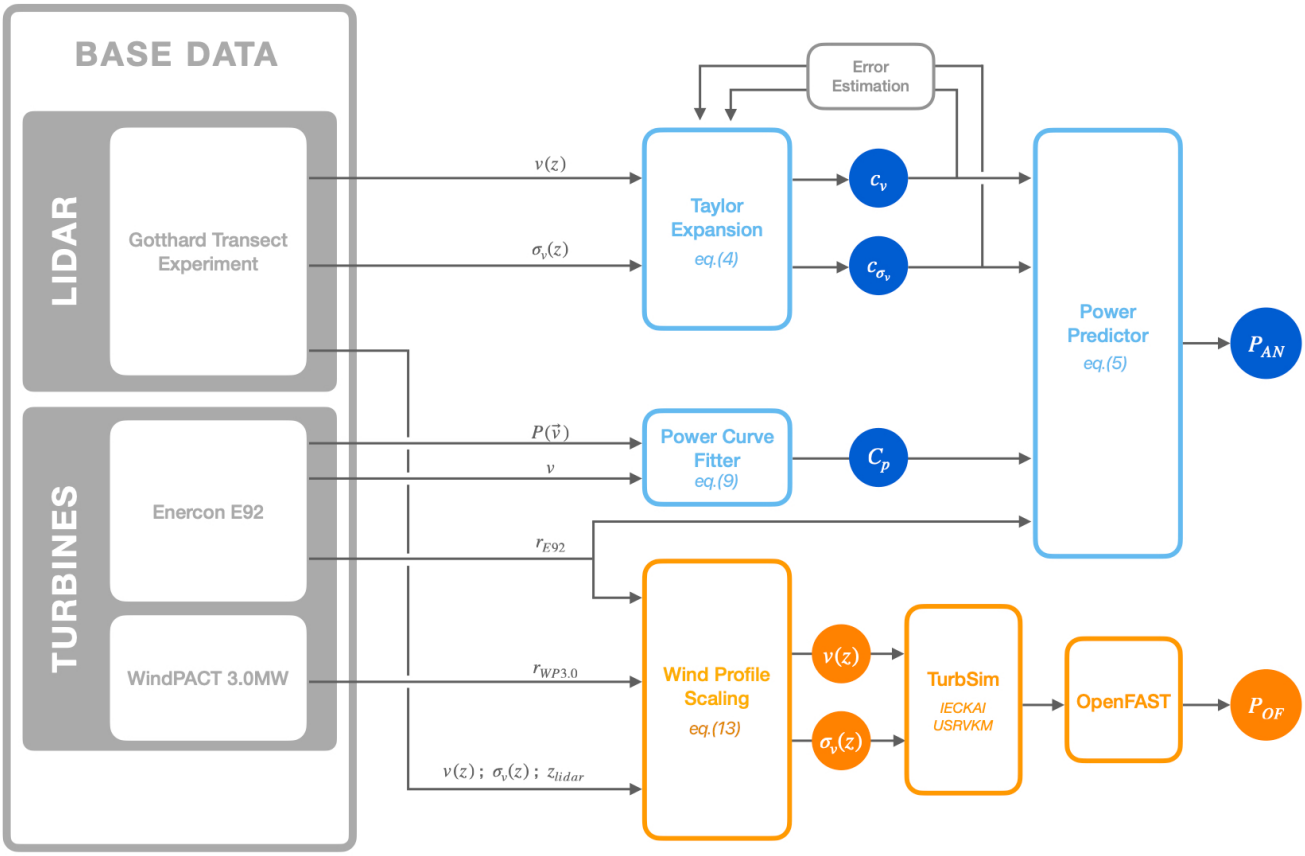


Figure 6. Schematic of the Analytical and OpenFAST model workflow.

2.4.2 Model intercomparison and evaluation

To evaluate the performance of the analytical model versus the OpenFAST simulations, we compare their predicted power output against the measured production of the five Enercon E92 turbines at the Gotthard Wind Park. Each turbine is assessed separately for the two prevailing wind direction (northerly and southerly), resulting in ten validations cases. For ~~every~~ each case, we ~~have selected a four hour~~ selected a four-hour window of 10-minute data, ~~which provides one~~ yielding 25 LiDAR-derived wind ~~profile from the nearest LiDAR location~~ profiles from the LiDAR location closest to the turbine, ~~and one~~ along with the corresponding turbine power ~~measurement per~~ measurements at each time step. An exception is LiDAR location 10 under northerly wind conditions, where only 6 profiles were available due to limited data.

For each of the ten cases, we compute the bias between the modelled and observed power over the 4 hour window. This results in a four bias estimates per case: analytical with and without turbulence, and OpenFAST with and without turbulence.

~~A single southerly case is excluded from this analysis due to the presence of a turbine wake, which is discussed separately in the results.~~

In addition to the per-case biases, we assess overall model skill by combining all (wake-free) cases and compute ~~RMSE, MAE and~~ Root Mean Square Error (RMSE), Mean Absolute Error (MAE), and the Coefficient of Determination; R-squared for each of the four model configurations. This pooled evaluation provides an overarching summary of model performance in varying ~~atmopsheric~~ atmospheric conditions and turbine responses in highly complex terrain.

Finally, we quantify model improvement using the relative reduction in bias between OpenFAST and the Analytical model as this is the key metric to model performance for each individual case. The global skill metrics are compared relatively between both models as well as the true measured power of the wind turbine. The inclusion of turbulence in the models is evaluated seperately to assess the importance of this additional variable.

This contrasts with the method used for the ~~idealised~~ idealized wind profiles, where we compare each profile to a uniform reference wind field to compute the power differences (ΔP) and isolate the contribution of each effect.

2.4.3 Wake Filtering

One single southerly case is excluded from the above-mentioned methodology due to the presence of a turbine wake. To better analyse this case, we used another useful feature of the Taylor-expanded wind profile which naturally enables the removal of anomalous or clearly unphysical measurements before constructing the analytical profile. This allows wake filtering even when data from adjacent, wake-free wind sectors are not available, as is often the case in strongly channelled flow environments such as the Gotthard wind park. Because our method relies only on a small number of vertically adjacent points, any range gates that contain erroneous values, such as flow disturbances caused by upstream turbine wakes, can simply be discarded with few consequences for the overall reconstruction of the wind profile.

This approach is appropriate either when the objective is to recover the undisturbed wind profile, or when the LiDAR happens to sit inside a wake while the turbine location of interest lies just outside of it. The Taylor expansion is then fitted to the remaining clean measurements immediately above and below the wake region, yielding an interpolated representation of the approximated undisturbed wind field. This special case is discussed separately in the results.

3 Results and Discussion

The following results assess the performance of the newly derived analytical model against both the IEC standard methods and high-fidelity OpenFAST simulations. Traditionally, the IEC standard approach relies on a single-point wind speed measurement, taken either at nacelle height or scaled from two-thirds of nacelle height, which neglects vertical wind profile variations. Our analytical model aims to overcome this limitation by explicitly accounting for vertical wind structure, while remaining computationally efficient.

We begin by ~~examining the differences in turbine power curves and their curvature, since these strongly influence how vertical variations in wind speed translate into power production. Next, we isolate the~~ isolating the effects of typical features of

vertical wind profiles, which includes shear, veer, and logarithmic wind profiles, as well as homogeneous turbulence intensity, through ~~idealised~~ the idealized wind profile test cases. We then apply the model to ten real-world cases applied to the five turbines at the Gotthard Pass, distinguishing between northerly and southerly flow conditions. Finally, we highlight one case strongly affected by wake interactions, and demonstrate how wake filtering can be applied to recover the undisturbed power signal and improve power prediction significantly.

3.1 ~~Differences in power curves~~

~~For the analytical model, we align with the Enercon E92 2.35 MW wind turbines installed at the Gotthard Wind Park. Power curve data is taken from the Enercon E92 specification sheet and is fitted (Equation 9), resulting in a smooth analytical expression (Fig. 3a).~~

~~Remaining with Figure 3, the OpenFAST simulations cannot be based on the Enercon E92 directly, as the required blade geometry to simulate power production is proprietary. Instead, the open-source WindPACT 3.0 MW turbine is used. This has consequences in all upcoming results since the turbine behaves differently due to the small variations in the shape of the powercurves. For example, the WindPACT turbine's $C_p(v)$ exhibits unrealistic features starting at extremely high values after which it remains unrealistically constant until the rated power is reached. Furthermore, the turbine power curve lacks defined cut-in and cut-out wind speeds, causing the model to produce power under wind conditions where a real turbine would not operate. This likely leads to an overestimation of energy production, particularly during very low and very high wind events.~~

~~Crucially, there is a difference in how these two power curves were derived; the Enercon E92 power curve results from long-term measurements which average over a large number of real wind profiles. This is strictly different form the WindPACT wind profile which is based on a uniform wind profile where v is constant with height, i.e. the reference case mentioned in 2.3. In reality the uniform wind profile assumption could be better represented by a logarithmic or power-law wind profile that more closely represents the wind profiles incident on the Enercon E92. However, this introduces an additional shear parameter (i.e. z_0 or α) that we can not accurately define as the wind profile information regarding the Enercon E92 power curve calibration was not reported. One could attempt to estimate this value knowing the test site topography, but uncertainties would remain as this shear parameter is largely influenced by atmopsheric stability and wind direction (Bot, 2016; Emeis, 2005).~~

~~Furthermore, the IEC 61400-12-1:2022 standard outlines that the power curve calibration – as performed for the Enercon E92 – requires the use of a nacelle-mounted LiDAR which performs a cubic-weighted average of the incoming wind field at nacelle height (IEC, 2022; Wagner et al., 2011). Considering that commercially available nacelle-mounted LiDARs tend to scan in a cone pattern, wind speed values from the entire swept area of the blade will be included in this averaging (Letizia et al., 2023; Rettenmeier et al., 2013). According to the standard, the nacelle-mounted anemometer shall be calibrated to this spatially cubic-weighted average windspeed. This would indeed convert the realistic, non-uniform wind profile into a single wind speed value, which can be treated as constant throughout the whole swept area of the wind turbine; in other words, a uniform flow profile.~~

~~Comparison of the Enercon E92 2.35 MW and WindPACT 3.0 MW powercurve, coefficient of performance and curvature. (a) Powercurves $P(v)$ and coefficients of performance $C_p(v)$, and (b) Curvature of the powercurves.~~

~~The powercurve's second derivative, representing the curvature, is shown in Figure 3b. This curvature is physically relevant, since it is directly responsible for the power production response on vertical wind speed variations across the swept area of the turbine. When parts of the turbine blade sweeps through different wind speed regimes, this curvature controls the degree to which these variations translate to power production. Notice the smooth curvature of the analytical Enercon E92 power curve, while the WindPACT 3.0 MW turbine exhibits a linear increase before an abrupt drop. The same features of linear power discrepancies and abrupt changes are observed throughout the following results.~~

3.1 ~~Idealised~~ Idealized wind profiles

The comparison between the power expectation from OpenFAST and the analytical model is summarised in Figure 7. For linear shear (Figure 7a), we find that shear effects contribute positively to the power production of the turbine in comparison to the homogeneous wind profile. The power estimated by the OpenFAST model consistently increases with shear, reflecting the cubic dependence of power on wind speed ($P \propto v^3$), where higher wind speed contribute more significantly to the overall output. Above the rated wind speed, ΔP tends to ~~0~~ 0 as the turbine saturates at its maximum capacity and the extra wind speed is not able to positively contribute to the power production. This is particularly well illustrated by the sudden drop of the OpenFAST curve at ~~$v = 12\,m\,s^{-1}$~~ $v = 12$. For the analytical model, the rated power is reached more smoothly at ~~$v = 14\,m\,s^{-1}$~~ $v = 14$ which can directly be attributed to the smoother curvature of the power curve as reported in Section~~2.2.1.~~ 2.2.1. With increasing shear coefficient a, we see similar increases in magnitude of ΔP for both models, and the peak values scale as expected with $\propto a^2$ as described in Equation 11.

Concerning the differences in the two models, we can observe two elements: the apparent overestimation of the analytical model, and the linear behaviour of the OpenFAST curve for low velocities. The overestimation of the power difference in the analytical model is most likely caused to the several reducing factors not taken into account in the analytical model. For example, the OpenFast considers the reduced efficiency of energy transfer from the wind to the turbine blade due to non-ideal angle of attack. Additional shearing forces and vibrations, that will inevitably cause additional friction and reduced power production in reality.

In the case of linear veer, shown in Figure 7b, the observations are analogous to the shear, but lead to a reduction in power output instead of an increase. This reduction arises from the diminished effective wind velocity component normal to the rotor plane, which is caused by the veer angle. The shape of both power difference curves are similarly more abrupt for the OpenFAST model due to the less refined and realistic power curve, and the analytical model reports higher differences due to a lack of dampening factors that are present in OpenFAST. As we vary the maximum veer angle $\alpha_{\max}$, the analytical model follows the expected square dependence ($\Delta P \propto \alpha_{\max}^2$) as described in Equation 12. The OpenFAST simulations, however, show slightly different magnitudes, with relatively larger power losses at smaller angles ($\alpha_{\max} = 5°$) and smaller losses at larger angles ($\alpha_{\max} = 22.5°$). This deviation is most likely due to the more detailed modelling of airflow over the blades, but it remains of secondary importance compared to the dominant quadratic dependence on $\alpha_{\max}$ in determining the overall turbine power output.

The ΔP curves of homogeneous turbulence, shown in Figure 7~~b~~c, has a characteristic shape which has previously been ~~reported~~ described to follow this relationship between power curve curvature and power contributions related to turbulence in similar works such as ~~?~~?. For low wind speeds, up to the inflection point of the power curve, turbulence tends to increase power production. This is because the turbulence velocity distribution, which is symmetric up to second order, places greater weight on velocity realisations above the mean. This holds true for the region in the power curve where the curvature is convex (i.e. positive in ~~Fig.~~Figure 3b), these higher velocities contribute disproportionately to the average power. Beyond the inflection point, however, the situation is reversed: the turbine response starts to saturate and the contribution of velocities below the mean becomes more significant than that of velocities above it. As a result, the net effect of turbulence is a reduction in power output.

The behaviour at the tail of the curve differs markedly between the two approaches. While the analytical model predicts no change in mean power above rated wind speed, the OpenFAST simulations show a small linear reduction. This behaviour is most plausibly explained by control-system and actuator dynamics under high turbulence: rapid fluctuations in effective angle of attack lead to persistent pitch-tracking errors (due to sensor/estimator lag, pitch-rate and torque limits, and ~~anti-windup), so the controller cannot hold the blades exactly at the optimum~~anti-wind-up). The controller likely simulates the rotor speed varying above and below the rated speed, where the power is clipped to a maximum on the positive variations, but not on the negative ones. The result is a small shortfall from the rated power ~~setpoint~~ set point that increases with turbulence intensity. Although our field dataset contains limited observations above rated wind speed, previous studies show that modern pitch-regulated turbines are designed to maintain constant power in this regime through active control adjustments ~~Rosmin et al. (2010); Sedaghat et al. (2016)~~(Rosmin et al., 2010; Sedaghat et al., 2016).

~~The final idealised~~ As we vary the turbulence intensity (TI), the magnitude of the turbulence-induced power variations increases in proportion to the second derivative of the power curve, as expected for both the analytical and OpenFAST models. A slight exception occurs for the OpenFAST model near the peak positive contribution to wind power around $v = 9.5$. With increasing TI, this peak shifts toward slightly lower wind speeds. This behaviour is likely due to the more detailed modelling of the flow over the turbine blades in OpenFAST and represents a secondary effect.

The final idealized profile which we will discuss is the logarithmic profile shown in Figure~~7e~~ 7d, a common profile that is used to describe the standard wind shear of the earth's surface. The curvature effects previously described for the linear shear still hold in this simulation. A noticeable observation is the relatively low impact of the logarithmic profile, with the maximum deviation from the uniform inflow amounting to only about 15 kW and 20 kW for the Analytical and OpenFAST models, respectively. The logarithmic profile resembles the linear shear profile in shape, however the increase in wind speed is more strongly limited than the decrease. So instead of a net positive effect, as might be expected from the convexity of the power curve, it results in a small negative effect. As discussed earlier in this ~~section~~Section, OpenFAST predicts this behaviour more abruptly, while the analytical model responds more smoothly. Interestingly, in this case the analytical model predicts a smaller magnitude of change. This is likely because, in the analytical formulation, the positive contributions more strongly compensate for the negative ones, whereas OpenFAST still simulations have additional sources of power loss due to friction and control dynamics of the turbine, compared to the baseline OpenFAST simulation.

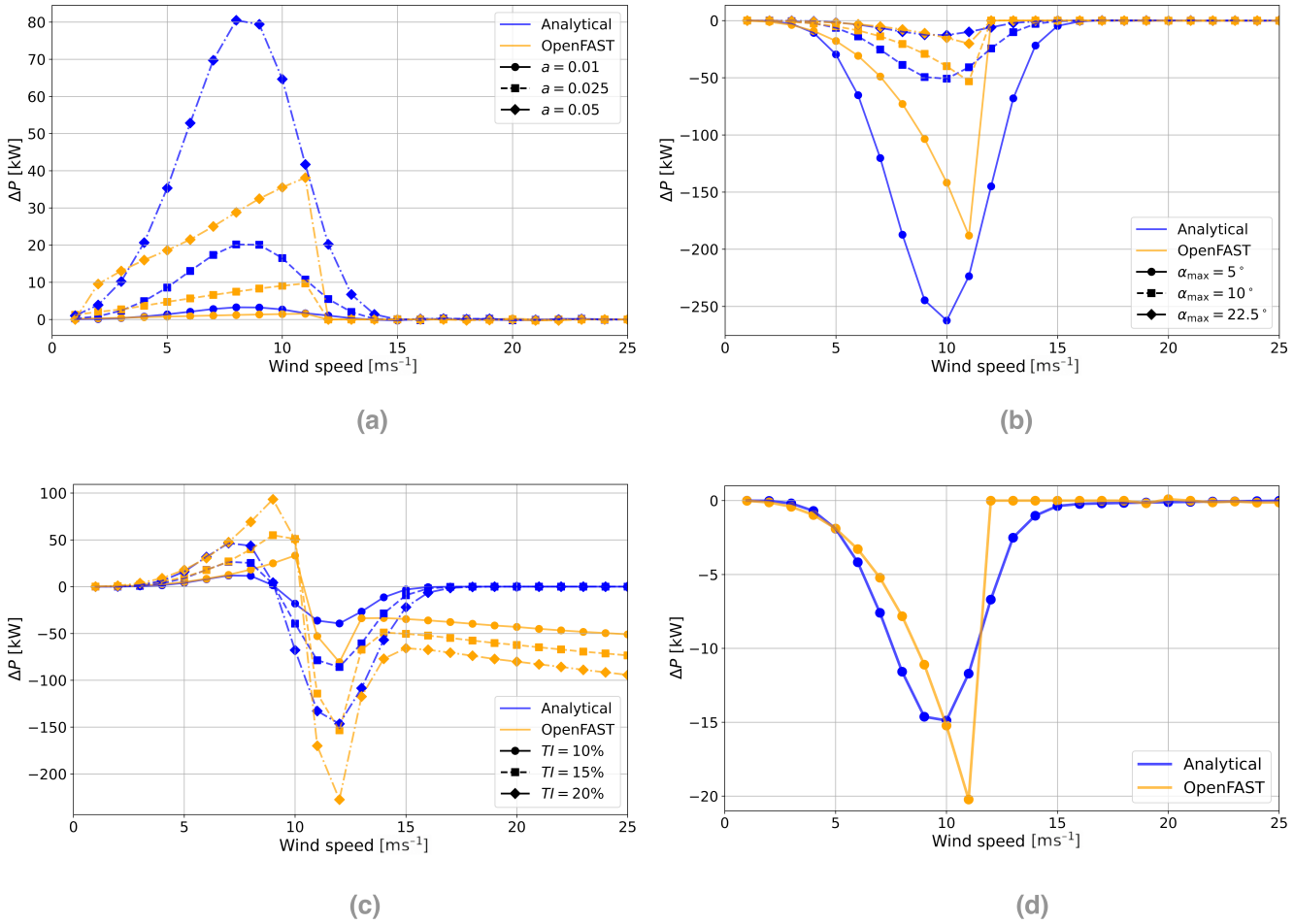


Figure 7. The difference in power production from a a uniform wind profile for the four ~~idealised~~ idealized vertical wind profiles. (a) Linear shear, (b) Linear veer, (c) Homogeneous turbulence intensity (TI), and (d) Logarithmic wind profile (~~$z_0 = 0.1\,m$~~ $z_0 = 0.1\,[\mathrm{m}]$).

3.2 Gotthard wind profiles

We continue by evaluating the models under real-world conditions. For this purpose we have selected ten distinct wind events at each of the five turbines in the Gotthard Wind Park. Each case spans several hours and is classified by southerly or northerly flow (~~Tab.~~ Table 2), which are the prevailing wind regimes for this mountain pass. For each event, we make use of the Gotthard Transect Experiment dataset ~~van Schaik et al. (2024)~~(van Schaik et al., 2024), which includes ten Doppler wind LiDAR deployments along the pass, providing upwind vertical wind profiles from all five turbines and prevailing winds.

In Figure 8, nine of the ten cases are shown; the case of Turbine 1 with LiDAR location 9 under southerly flow is omitted. The wake effects from Turbine 2 contaminating the LiDAR wind profiles before reaching Turbine 1 requires a separate case. This special case is discussed in ~~subsection~~ Subsection 3.3.

The first ~~subfigure (Fig.~~ sub-figure (Figure 8a) compares the predicted and observed power output, with the turbulence module enabled for both models. As observed before in ~~Fig.~~ Figure 7c, the turbulence improves power output until about $10\,m\,s^{-1}$, after which power production is decreased, reducing deviation from the true power in all cases. Compared to the turbulence-free case (~~Fig.~~ Figure 8b), this model version achieves ~~much~~ slightly better agreement with the measured power production ~~, particularly at high wind speeds~~which only becomes clear when considering the bias values in Table 2. Here, the analytical model clearly outperforms OpenFAST, which often overestimates power once the rated power of the turbine is reached. This behaviour can also be observed from the ~~idealised~~ idealized wind profiles of Figure 7.

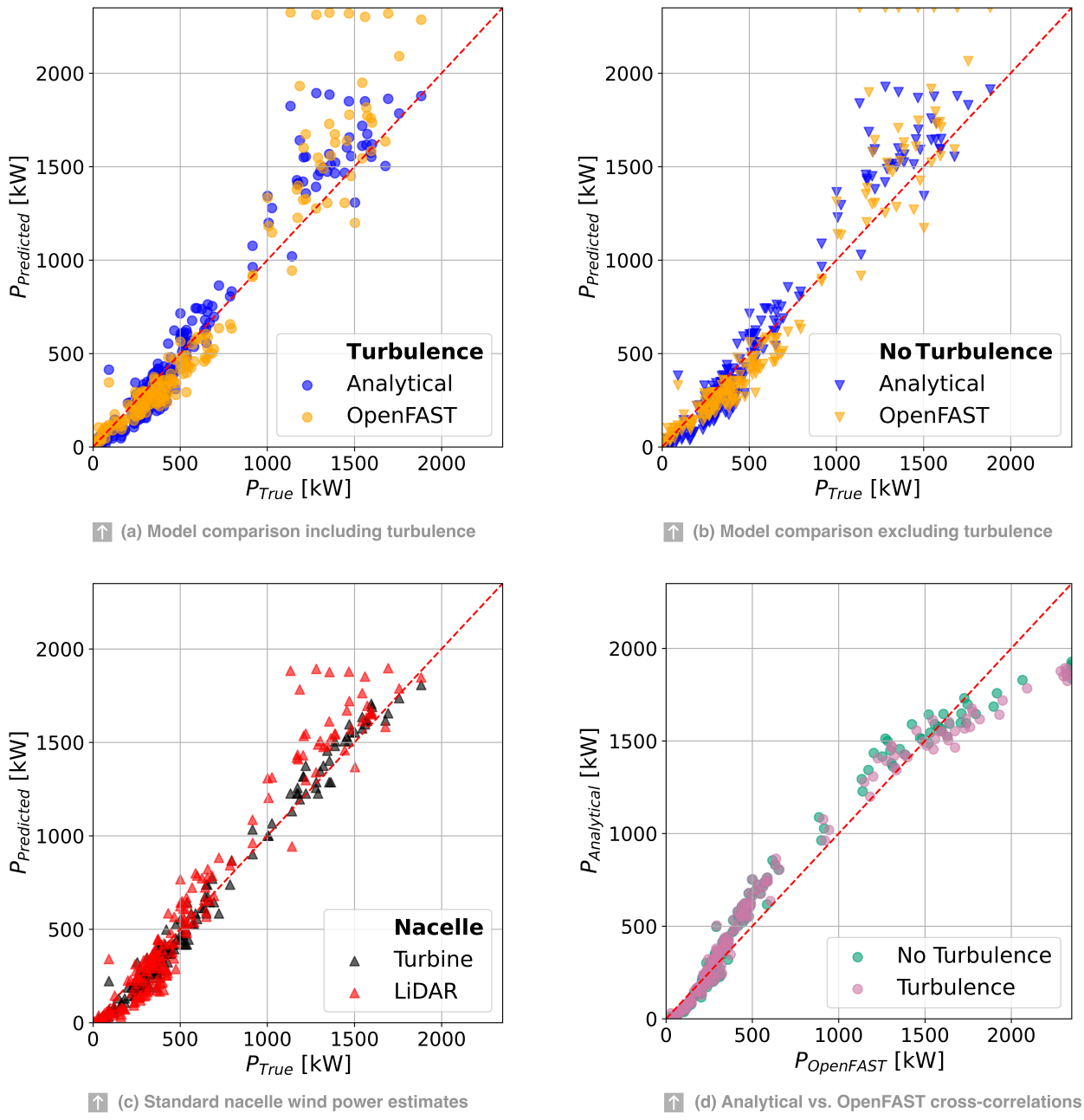


Figure 8. The ~~difference~~ differences in power production from ~~a a uniform wind profile for~~ the ~~four idealised vertical wind profiles~~Analytical and OpenFAST models, and compared to standard approaches. (a) Comparison ~~incl.~~ of the two models including turbulence and (b) ~~excl.~~ excluding turbulence. (c) Standard nacelle power estimates from turbine anemometer and LiDAR and (d) Model cross-correlations.

In Figure~~8.~~ 8d, the cross-correlation between the analytical and OpenFAST models are shown. A systematic pattern can be observed here. Firstly, at very low wind speeds, OpenFAST generates power earlier because it lacks a defined cut-in wind speed – a known unrealistic feature of the software. This should however not affect the results in a measurable way as the selected cases do not include the trivial case where $v < v_{in}$ where $P = 0\,\mathrm{kW}$. Secondly, in the intermediate region, the analytical model produces more power due to the stronger curvature of the power curve (~~Fig.~~Figure 3b). Finally, at higher wind speeds, OpenFAST diverges again to greater power predictions, reflecting its unrealistic post-rated behaviour. Notably, the inclusion of turbulence only has a significant impact near rated power as the power curve flattens afterwards.

To connect these findings of the power prediction models to the IEC standard methods, the third ~~subfigure (Fig. 8~~sub-figure (Figure 8c) shows predictions based on nacelle-height wind speed alone. The trivial case is the turbine nacelle measurement itself (black), which unsurprisingly correlates well with true power since it is effectively calibrated against it. Still, small deviations indicate the importance of vertical variations in the inflow. More striking is the performance of the LiDAR-based nacelle-height estimations (red), which effectively serve as the IEC-standard extrapolation method. In this case, we have data available at the nacelle-height, but the IEC standard only allows for measurements from up to two-thirds of hub-height to be extrapolated for this purpose. When considering the variety of the wind profiles measured by the LiDAR on the Gotthard pass, it becomes immediately evident that there is no single surface roughness that can be assigned to this site to perform such an extrapolation. We therefore remain at the best possible case for the IEC standard by taking the LiDAR range gate closest to the elevation of the nacelle. Relative to the IEC standard approach, the analytical model reports several improvements with the inclusion of the vertical wind profiles.

Table 2. Specification and error statistics of the ten Gotthard case study sites

Case study site			LiDAR–Turbine	Number of	Bias from measured power [kW]			
Turbine	LiDAR	Wind direction	distance	wind profiles	Analytical	An. No-turb.	OpenFAST	IEC Standard
T1	L9	Northerly	207 m	25	-13.7	-26.4	-50.2	-25.6
T1	L9	Southerly		25	-242.9*	-267.9*	-468.7	-555.5
T2	L5	Northerly	278 m	25	223.7	256.6	412.0	254.8
T2	L6	Southerly		25	-20.9	-25.2	-10.6	-26.0
T3	L10	Northerly	116 m	6	-32.9	-46.4	-79.6	-55.5
T3	L10	Southerly		25	-27.8	-37.4	17.2	-39.1
T4	L4	Northerly	156 m	25	130.9	158.2	154.5	141.9
T4	L4	Southerly		25	-13.1	-26.4	-53.9	-20.0
T5	L7	Northerly	114 m	25	67.8	64.7	-86.8	103.0
T5	L7	Southerly		25	-105.9	-121.6	-71.9	-133.7
				RMSE [kW]	140.3	150.5	215.7	153.8
				MAE [kW]	95.0	103.5	121.0	108.1
				R^2	0.911	0.897	0.794	0.893

* Corrected for wake effects

As shown in Table 2, the wind power bias reduction per site relative to the IEC standard ranges from ~~8.6% to 46.4%~~ 8.6 % to 46.4 %, depending on site complexity, with a mean bias reduction of ~~25.4 ± 13.0%.~~ 25.4 ± 13.0 %. The bias reduction is computed as the relative difference between the analytical approach and the IEC standard, defined as (Analytical − IEC)/IEC, using the corresponding bias values from the first and last column of the Bias section of Table 2. This improvement directly translates to a more accurate prediction of turbine power production: the analytical model yields production estimates that are on average ~~5.4 ± 3.8%~~ 5.4 ± 3.8 % closer to observed values. Across the sites, this corresponds to improvements ranging from ~~0.86% to 14.1%~~0.86 % to 14.1 %. For the Gotthard Pass Enercon E-92 turbines, this equates to an average of ~~23.7 *MWh*~~ 23.7 MWh per turbine closer to the true annual energy production. In terms of statistical error metrics, the analytical model reduces the RMSE by ~~8.8%~~8.8 %, and the MAE by ~~12.2%~~ 12.2 % compared to the IEC standard. However, the OpenFAST power predictions are consistently worse than the LiDAR nacelle-height wind speed method. This discrepancy can be single-handedly attributed to the different wind turbine used in the simulations, as the proprietary aerodynamic specifications of the Enercon E92 prevent its implementation in OpenFAST. Instead, the open-source WindPACT 3.0 MW turbine had to be employed and scaled, introducing systematic differences that affect the comparability of results.

In these OpenFAST simulations of the Gotthard wind profiles, the *USRVKM* turbulence mode in TurbSim was used, providing vertical turbulence variations and the ability to specify eddy length scales, unlike the *IECKAI* mode used for the ~~idealised~~ idealized profiles. Sensitivity tests across a range of turbulence intensities and eddy scales showed only minor effects on power

predictions, primarily at high wind speeds. Given that the analytical model already demonstrates superior performance, the standard *USRVKM* settings were retained.

Overall, the results show that while nacelle-height extrapolation can provide reasonable fits, the analytical model generalises significantly better for complex terrain site assessments. Including turbulence further sharpens its predictive skill, particularly at high wind speeds, while retaining negligible computational cost compared to OpenFAST.

3.3 Wake filtering

In Figure 9a, the original LiDAR wind measurements from LiDAR location 9 for southerly wind conditions, relative to Turbine 1, are shown in orange, together with a subset of ~~selected points~~ points selected outside the wake-contaminated region.From the analysis of wake direction and extent, this case was identified as the only instance where either the LiDAR or the turbine is affected by a wake. Specifically, for Turbine 1 and LiDAR location 9 under southerly wind conditions, the wake from Turbine 2 intersects the LiDAR beam but consistently bypasses Turbine 1. This becomes evident when considering the turbine position angle of Turbine 2: extending a line downstream on the lee side of the turbine, while accounting for the swept area of the rotor, shows that the wake passes over LiDAR location 9 but does not intersect Turbine 1. As a result, the LiDAR profile misrepresents the true inflow conditions of the turbine.

The error bars of both the orange and green profiles, as well as the shaded blue region, represent the standard deviation of the wind speed, during the 10 min time window in which complete wind profiles are measured every 5 seconds. After wake filtering, the resulting profile (blue) behaves much more consistently as if no wake was present, which is also observed by the reduced turbulence intensity, also interpolated by the Taylor expansion.

The effect on power predictions due to the filtering of the wake is shown in Figure 9b. The unfiltered case, with analytical and OpenFAST predictions in blue and orange respectively, substantially underestimates the measured turbine power. After applying the wake filter, the analytical results align much more closely with the actual turbine production. Quantitatively, the RMSE decreases from ~~515.8 *kW* to 242.9 *kW*~~515.8 kW to 242.9 kW, which is a reduction of ~~53%~~53 %, while the bias ~~improves from 58% to −215.3 *kW*~~is reduced by 58 % to -215.3 kW. The only trade-off is a slight decrease in correlation, from 0.55 to 0.50, indicating that the effectiveness of the wake correction varies between individual profiles. This is to be expected as the procedure simply removes a standard range of wind measurements where the wake is expected based on the height of the swept area of Turbine 2 with respect to the elevation of the LiDAR. In some cases, particularly when the wind field contains a vertical component, wake remnants may still contaminate the higher points, or the correction may overcompensate, as visible in one outlier above the $1:1$ line.

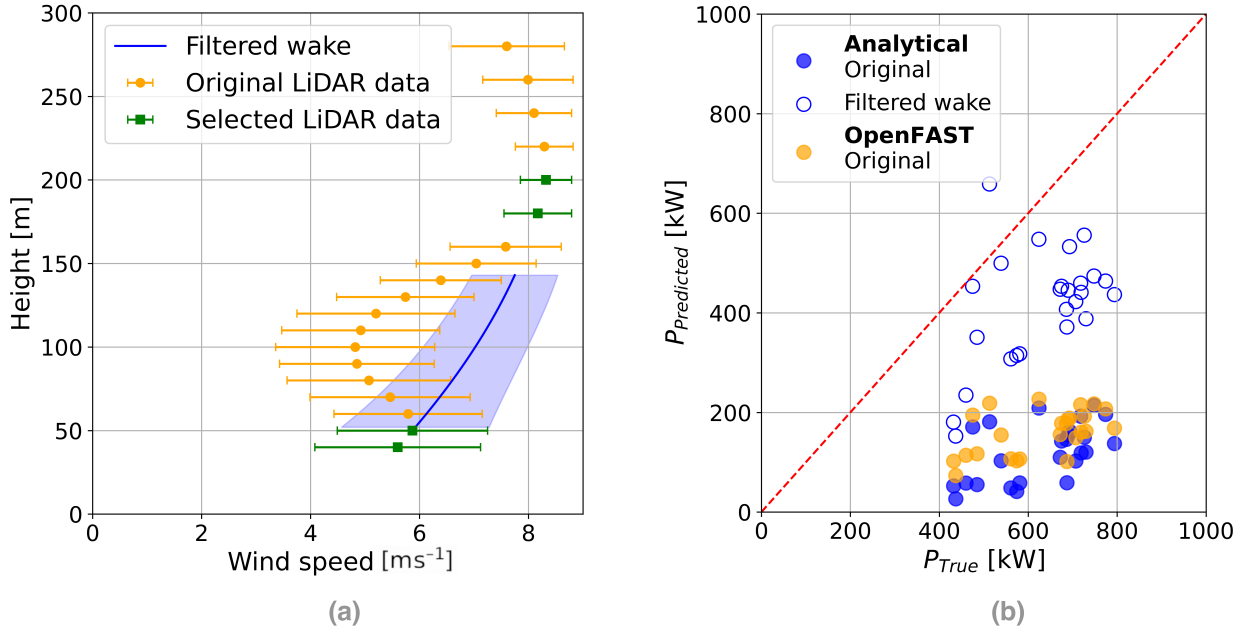


Figure 9. Wake filtering of LiDAR location 9 with Turbine 1 under Southerly winds (a) wind profile and (b) power production comparison.

Despite these limitations, the approach works remarkably well and highlights a key advantage of the analytical model: it can be applied flexibly to almost any kind of input data. Whether only two measurement levels are available or a densely resolved LiDAR profile, the Taylor expansion method adapts naturally. This stands in stark contrast to to the OpenFAST method which cannot directly accommodate such filtering. Importantly, the method is also turbine-independent: even before a specific turbine type is selected, a single LiDAR deployment can provide accurate wind energy assessments for any size turbine. Furthermore, wake-filtered profiles can be particularly valuable in cases such as wind farm expansions, where wake contamination is unavoidable, yet filtering offers a practical way to recover representative inflow profiles such as in off-shore applications where one can expect the uneffected wind profile to be similar within a few kilometres from the LiDAR site.

3.4 Robustness and Sensitivity Tests

In addition to the core results, several supplementary tests were conducted to evaluate the robustness of the analytical model. First ~~, the~~ the shaft tilt, which is set to 0° in the numerical simulations to stay consistent with the analytical method, was tested to the more realistic 5° which can be found in the Enercon E92 technical specifications. This introduces a small bias of approximately 8 kW for the 2.35 MW turbine. However, since the wind profile is based on a LiDAR measurement located roughly 100 m from the turbine, any slight decrease in horizontal inflow or the inclusion of vertical wind components caused by shaft tilt would not significantly improve the accuracy. Therefore, we chose to retain the simpler configuration which are comparable to the idealized wind profiles.

Secondly, the sensitivity to air density was investigated using OpenFAST simulations across a range of values representative for wind parks at different elevations. The analytical model was found to be well behaved across the full range, with no need to adjust the shape of the $C_p(v)$ curve, confirming its transferability to sites at different elevations.

~~Secondly~~Thirdly, we tested the impact of using alternative turbine power curves. When replacing the Enercon E-92 curve with the WindPACT 3.0 MW reference turbine, the agreement between the analytical model and OpenFAST became closer, although this improvement was primarily due to a degradation of the analytical model rather than an enhancement of OpenFAST. This illustrates that the framework can be applied to arbitrary power curves, as the analytical approximation in ~~Eq.~~Equation 9 is flexible and well behaved.

Finally, we assessed the impact of temporal averaging on estimates of $\overline{v^3}$ by ~~re-averaging~~ aggregating the 1 s LiDAR wind-speed data ~~to~~ over a range of averaging ~~windows~~ intervals (1, 2, 5, 10, 20, and 30 minutes, and 1 hour). ~~For otherwise comparable conditions, the resulting values of $\overline{v^3}$ differed by up to 4% relative to estimates based on $\overline{v}$, illustrating the sensitivity of power-related metrics to the chosen averaging interval. Since 10-minute averages remain the standard in~~ Changing the averaging window slightly modifies the resulting wind profiles, which in turn affects the analytically derived power production. We find that these differences remain relatively small, on the order of 4 %. While this effect is not explored further, it is worth noting as a minor source of uncertainty. In line with standard wind-energy ~~applications, we adopt them here, while noting that this choice introduces a small but unavoidable uncertainty in the order of several percent.~~ practice, 10-minute averages are adopted throughout this study.

Together, these tests demonstrate that the analytical model is robust to variations in air density and turbine power curves, and that averaging effects introduce only a limited and unavoidable contribution to the overall error budget.

4 Conclusions

In this study, we introduced and validated a new analytical framework for predicting wind turbine power production that explicitly accounts for vertical wind profile variability through an integral formulation. By combining Taylor expansions of the inflow with an analytical representation of the turbine power curve, the model provides a clearly improved alternative to the IEC standard for wind energy assessment based on a single nacelle-height wind measurement. Furthermore, it provides a flexible alternative to costly numerical simulation of wind turbine aerodynamics.

The results show that the primary discrepancies between the analytical model and OpenFAST can be attributed to differences in the turbine power curves. While the analytical model was configured for the Enercon E-92 turbine, reflecting the real-world LiDAR measurements at the Gotthard Pass, OpenFAST required the use of the WindPACT 3.0 MW reference turbine. The unusual $C_p(v)$ curve of the latter, including the absence of realistic cut-in and cut-out wind speeds, amplified differences in the response to vertical wind profile variations. This effect is best represented by considering the curvature ($\frac{d^2P}{dv^2}$) of the power curve, which confirms the mechanism and provided an explanation for the observed discrepancies in the predicted power of the turbines.

When applying the analytical model to ~~idealised~~ idealized wind profiles, such as linear shear -, linear veer-, logarithmic wind profiles, as well as homogeneous turbulence intensities, we demonstrated that the analytical formulation produces smoother and more physically consistent power predictions compared to OpenFAST. These differences are likely driven by the different power curves.

This same effect is also visible in the real Gotthard LiDAR profiles, which provided a direct validation against real-world inflow conditions. The vertical wind profiles at this alpine site are strongly shaped by shear, veer, and turbulence, and represent a complex but highly relevant test case for wind energy production. Compared to OpenFAST, the analytical model showed smoother and more consistent responses to these profiles, reflecting the more regular curvature of the Enercon E-92 power curve used in its formulation. Resulting in remarkably high goodness of fit of $R^2 = 0.911$, with typical bias reduction of ~~$25.4 \pm 13.0\%$~~ 25.4 ± 13.0 % which corresponds to an annual average of ~~$23.7\ MWh$~~ 23.7 MWh per turbine (Enercon E92 2.35 MW) closer to the true production power for this highly complex Alpine site.

The wake filtering analysis further illustrated the strength of the analytical approach by means of its flexibility: By excluding the portion of the LiDAR profile affected by a turbine wake, the analytical model predictions were brought significantly closer to the measured power, reducing the RMSE and Bias by more than ~~50%~~50 %, significantly closer to the typical skill of the other cases. Although, the slight decrease in correlation suggests that this method does not work as effectively on every wind profile due to leaking over wake effects. Further work should consult the plethora of literature available on wake detection, which will likely be the remedy to this rather straight-forward problem that is outside of the scope of this work.

Further robustness and sensitivity tests confirmed that the analytical framework performs consistently across a range of air densities representative of all elevations, and that the method can be applied to arbitrary power curves thanks to the analytical approximation of ~~Eq.~~ Equation 9. Furthermore, we have conducted tests on the sensitivity of the 10-minute averaging window which has become state-of-the-art in the wind energy industry and conclude that this does introduce a small additional, and probably unavoidable, uncertainty of up to ~~4%~~ 4 % in the power prediction. This effect is minor not of interest to study further given the trade-off with turbulence statistics.

In summary, the analytical model developed here applies a simple physical interpretation of vertical variations in the wind in a computationally efficient and highly flexible tool for assessing turbine power production under vertically varying wind conditions. It captures the essential mechanisms behind power output variations, explains discrepancies with simulation-based models through power curve curvature, and can be robustly applied across sites, turbines and measurement configurations. Beyond its application in the Swiss Alps with the Gotthard Pass case study, the model offers a new pathway to bridge measurements that we think should be considered to be amended in today's wind energy assessment standards, as it is low impact due to our open-source code for the tool, and the trend of using LiDAR in site selection for wind parks which already include this additional information of vertical wind profiles. We particularly want to highlight the value in the practicality of use in the majority of cases where wind turbine aerodynamic specifications are proprietary. Something that more sophisticated simulations and other state-of-the-art tools require, which is completely avoidable by this method.

Code and data availability. All data is publicly available via the Zenodo database (van Schaik et al., 2025a) doi: https://doi.org/10.5281/zenodo.17804408. With the single exception of the Gotthard Wind Park Turbine Power data, which was used under Non-Disclosure Agreement. This data may be made available under request to the authors for scientific purposes only. The Zenodo database additionally includes open source code for the analytical power prediction tool as well as example codes and instructions to operate the software.

Appendix A: Analytical power equation derivation

From Taylor series theory, a continuous function such as the wind speed profile can be approximated by a polynomial:

$$v(z) = \sum_{i=0}^{N} c_i z^i \tag{A1}$$

The standard turbine power equation is:

$$P(z) = \frac{1}{2} C_p(v) \rho A v(z)^3 \tag{A2}$$

We integrate over the circular swept area by converting the surface integral to a 1D integral in height:

$$P = \frac{1}{2} C_p(v) \rho \int_{-R}^{R} 2\sqrt{R^2 - z^2}\, v(z)^3 \, dz dz \tag{A3}$$

To integrate over the height z, we must define the cube of the wind speed that is parallel to the normal vector of the swept area:

$$(v(z))^3 = \sum_{i,j,k i,j,k=0}^{N} c_i c_j c_k z^{i+j+k} = \sum_{i i=0}^{N} \left(c_i \sum_{j j=0}^{N} \left(c_j \sum_{k k=0}^{N} \left(c_k z^{i+j+k} \right) \right) \right) \tag{A4}$$

~~Such that we can define the turbine power equation as a integral over height z.~~

$$P(v,z) = \frac{1}{2} C_p(v) \rho \int_{-R}^{R} 2\sqrt{R^2 - z^2}\, v(z)^3 dz$$

We solve this analytically by the following subtitution:

$$z = R sin R \sin(u),\ u = arcsin \arcsin\left(\frac{z}{R}\right), dz = R cos R \cos(u) du \tag{A5}$$

Such that the power equation becomes:

$$P(v,u) = \frac{1}{2} C_p(v) \rho \int_{\frac{-\pi}{2}}^{\frac{\pi}{2}} 2R cos 2R \cos(u) \sqrt{R^2 - R^2 sin^2(u)} \sqrt{R^2 - R^2 \sin^2(u)} \sum_{i,j,k i,j,k=0}^{N} c_i c_j c_k R^{i+j+k} sin \sin^{i+j+k}(u) du du \tag{A6}$$

Simplifying by removing the factor 2 out of the integral, and by rearranging the square root:

$$P(v,u) = C_p(v)\rho \int_{\frac{-\pi}{2}}^{\frac{\pi}{2}} Rcos R\cos(u)\sqrt{R^2(1-sin^2(u))}\sqrt{R^2(1-\sin^2(u))}\sum_{i,j,k\,i,j,k=0}^{N} c_i c_j c_k R^{i+j+k} sin\sin^{i+j+k}(u) du du \tag{A7}$$

The square root can be resolved by a trigonometric substitution to find:

$$P(v,u) = C_p(v)\rho \int_{\frac{-\pi}{2}}^{\frac{\pi}{2}} R^2 cos\cos^2(u)\sum_{i,j,k\,i,j,k=0}^{N} c_i c_j c_k R^{i+j+k} sin\sin^{i+j+k}(u) du du \tag{A8}$$

We can move the triple summation, including several constants out of the integral to simplify the integral to a purely trigonometric problem:

$$P(v,u) = C_p(v)\rho R^2 \sum_{i,j,k\,i,j,k=0}^{N} c_i c_j c_k R^{i+j+k} \int_{\frac{-\pi}{2}}^{\frac{\pi}{2}} cos\cos^2(u)\, sin\sin^{i+j+k}(u) du du \tag{A9}$$

We now focus on the integral only, by defining it as ~~Q:~~ Q_m:

$$P(v,u) = C_p(v)\rho R^2 \sum_{i,j,k\,i,j,k=0}^{N} c_i c_j c_k R^{i+j+k} Q_m(u) \tag{A10}$$

Where the substitution $Q(z)$ also replaces $i+j+k$ by a new integer m:

$$Q_m(u) = \int_{\frac{-\pi}{2}}^{\frac{\pi}{2}} cos\cos^2(u)\, sin\sin^m(u) du du,\ m = i+j+k \tag{A11}$$

For odd values of m, the integrand $\cos^2(u)\sin^m(u)$ is an odd function, and the integral over the symmetric interval $[-\pi/2, \pi/2]$ evaluates to ~~0:~~ 0:

$$Q_m(u) = 0, \quad \text{if } m \text{ is odd.} \tag{A12}$$

For even values of m, let $m = 2s$, where s is an integer. The integrand $\cos^2(u)\sin^{2s}(u)$ an even function, and by symmetry, the integral can be simplified by doubling the range from $[0, \pi/2]$:

$$Q_m(u) = 2\int_{0}^{\frac{\pi}{2}} \cos^2(u)\sin^{2s}(u)\, du du, \quad \text{if } m = 2s. \tag{A13}$$

We once again apply the trigonometric identity to eliminate the cosine from the integrand.

$$Q_m(u) = 2\int_{0}^{\frac{\pi}{2}} \left(1-\sin^2(u)\right)\sin^{2s}(u) du du, \quad \text{if } m = 2s. \tag{A14}$$

~~We can split this integral in two relatively simple integrals:~~

Using $1-\sin^2(u)=\cos^2(u)$, this becomes:

$$Q_m(u) = 2\int_0^{\frac{\pi}{2}} \sin^{2s}(u)\,du - \int_0^{\frac{\pi}{2}} \sin^{2(s+1)}\cos^2(u)du, \quad \text{if } m=2s\,du. \tag{A15}$$

~~Which are both similar integrals as the exponent of the sign is always even. The integral of $\sin^{2s}(u)$ over the interval $[0,\pi/2]$ is given by:~~

This integral directly corresponds to the Beta function, yielding:

$$\int_0^{\frac{\pi}{2}} \sin^{2s}Q_m(u)\,du = \frac{1}{2}B\left(s+\frac{1}{2},\frac{1}{2}\frac{3}{2}\right),. \tag{A16}$$

where ~~$B(x,y)$~~ $B(x,y)$ is the Beta function~~. Using the relationship between the Beta and Gamma functions:~~

$$B(x,y) = \frac{\Gamma(x)\Gamma(y)}{\Gamma(x+y)},$$

~~the integral can be written as:~~

$$\int_0^{\frac{\pi}{2}} \sin^{2s}(u)\,du = \frac{\sqrt{\pi}}{2}\cdot\frac{\Gamma\left(s+\frac{1}{2}\right)}{\Gamma(s+1)}.$$

~~Here, $\Gamma(z)$ is the Gamma function, and $\Gamma\left(\frac{1}{2}\right)=\sqrt{\pi}$~~, defined as $B(x,y)=\frac{\Gamma(x)\Gamma(y)}{\Gamma(x+y)}$.

Such that ~~$Q(u)$~~$Q_m(u)$, for even values of $m=2s$, is given by:

$$Q_m(u) = \sqrt{\pi}\left(\frac{\Gamma\left(s+\frac{1}{2}\right)}{\Gamma(s+1)} - \frac{\Gamma\left(s+\frac{3}{2}\right)}{\Gamma(s+2)}\right) \tag{A17}$$

And the turbine power equation is given by:

$$P(v) = C_p(v)\rho R^2 \sum\nolimits_{i,j,k\,i,j,k=0}^{N} c_i c_j c_k R^m \sqrt{\pi}\left(\frac{\Gamma\left(s+\frac{1}{2}\right)}{\Gamma(s+1)} - \frac{\Gamma\left(s+\frac{3}{2}\right)}{\Gamma(s+2)}\right) \quad m=2s=i+j+k\,|\,m \text{ is even} \tag{A18}$$

Which is only a function of wind speed v again.

The Gamma function ~~$\Gamma(z)$~~$\Gamma(x)$, is defined by:

$$\Gamma(zx) = \int_0^\infty t^{z-1} e^{-t}\, dtdt \tag{A19}$$

For positive integers, where ~~$z = s = m/2 = (i+j+k)/2$~~ $x = s = m/2 = (i+j+k)/2$ (with m the sum of the three positive integers), the Gamma function simplifies as:

$$\Gamma(m) = (m-1)! \tag{A20}$$

To evaluate the Gamma function at half-integer values, consider $z = m + \frac{1}{2}$, where m is a non-negative integer. The key idea comes from using the recursive property of the Gamma function and its relationship with the factorial for half-integer arguments.

Using the reflection formula and the recurrence relation:

$$\Gamma\left(\frac{1}{2}\right) = \sqrt{\pi} \tag{A21}$$

and for higher half-integer values, you apply the recurrence relation $\Gamma(z+1) = z\Gamma(z)$ repeatedly. ~~For example:~~

$$\Gamma\left(\frac{3}{2}\right) = \frac{1}{2}\Gamma\left(\frac{1}{2}\right) = \frac{1}{2}\sqrt{\pi}$$

$$\Gamma\left(\frac{5}{2}\right) = \frac{3}{2}\Gamma\left(\frac{3}{2}\right) = \frac{3}{2}\cdot\frac{1}{2}\sqrt{\pi} = \frac{3}{4}\sqrt{\pi}$$

$$\Gamma\left(\frac{7}{2}\right) = \frac{5}{2}\Gamma\left(\frac{5}{2}\right) = \frac{5}{2}\cdot\frac{3}{4}\sqrt{\pi} = \frac{15}{8}\sqrt{\pi}$$

The general result for half-integer values of $\Gamma\left(n + \frac{1}{2}\right)$ (where n is a non-negative integer) is:

$$\Gamma\left(s + \frac{1}{2}\right) = \frac{(2s)!}{4^s s!}\sqrt{\pi} \tag{A22}$$

Thus, the Gamma function evaluated at half-integers $s + \frac{1}{2}$ is a product of a factorial expression, $\sqrt{\pi}$, and powers of 4.

Such that finally we can replace the full integer Gamma functions

$$P(v) = C_p(v)\rho\sqrt{\pi}R^2 \sum\nolimits_{i,j,k\, i,j,k=0}^{N} c_i c_j c_k R^m \left(\frac{\Gamma(s+\frac{1}{2})}{s!} - \frac{\Gamma(s+\frac{3}{2})}{(s+1)!}\right), \quad m = 2s = i+j+k \,|\, m \text{ is even} \tag{A23}$$

We apply the recurrence relation on the $\Gamma(s+\frac{3}{2})$:

$$P(v) = C_p(v)\rho\sqrt{\pi}R^2 \sum\nolimits_{i,j,k i,j,k=0}^{N} c_i c_j c_k R^m \left(\frac{\Gamma(s+\frac{1}{2})}{s!} - \frac{(s+\frac{1}{2})\,\Gamma(s+\frac{1}{2})}{(s+1)!} \right), \quad m = 2s = i+j+k \,|\, m \text{ is even} \tag{A24}$$

We rearrange to a single Gamma function:

$$P(v) = C_p(v)\rho\sqrt{\pi}R^2 \sum\nolimits_{i,j,k i,j,k=0}^{N} c_i c_j c_k R^m \left(\frac{(s+1)! - s!(s+\frac{1}{2})}{s!(s+1)!} \Gamma\left(s+\frac{1}{2}\right) \right), \quad m = 2s = i+j+k \,|\, m \text{ is even} \tag{A25}$$

Reduce the $(s+1)!$ to $s!(s+1)$:

$$P(v) = C_p(v)\rho\sqrt{\pi}R^2 \sum\nolimits_{i,j,k i,j,k=0}^{N} c_i c_j c_k R^m \left(\frac{s!(s+1) - s!(s+\frac{1}{2})}{s!(s+1)!} \Gamma\left(s+\frac{1}{2}\right) \right), \quad m = 2s = i+j+k \,|\, m \text{ is even} \tag{A26}$$

Which cancels out the $s!$:

$$P(v) = C_p(v)\rho\sqrt{\pi}R^2 \sum\nolimits_{i,j,k i,j,k=0}^{N} c_i c_j c_k R^m \left(\frac{1}{2} \frac{1}{(s+1)!} \Gamma\left(s+\frac{1}{2}\right) \right), \quad m = 2s = i+j+k \,|\, m \text{ is even} \tag{A27}$$

We finally use the general result for half-integer values of the ~~Gamme~~ Gamma function to find:

$$P(v) = C_p(v)\rho\pi R^2 \sum\nolimits_{i,j,k i,j,k=0}^{N} c_i c_j c_k R^m \frac{1}{2} \frac{1}{(s+1)!} \frac{(2s)!}{4^s s!}, \quad m = 2s = i+j+k \,|\, m \text{ is even} \tag{A28}$$

Where the $\sqrt{\pi}$ reunites with the other $\sqrt{\pi}$ to arrange $A = \pi R^2$ which obviously refers to the swept area of the blade A. We also replace s with $m/2$:

$$P(v) = C_p(v)\rho\pi R^2 \sum\nolimits_{i,j,k i,j,k=0}^{N} c_i c_j c_k R^m \frac{1}{2} \frac{1}{(\frac{m}{2}+1)!} \frac{m!}{2^m \frac{m}{2}!}, \quad m = i+j+k \,|\, m \text{ is even} \tag{A29}$$

Some final mathematical book-keeping where the half is moved to the front and πR^2 is combined to reflect the regular expression of the power equation, and by rearranging the factorials and exponents of 2, results in

$$\boxed{P(v) = \frac{1}{2} C_p(v)\rho A \sum_{i,j,k=0}^{N} c_i c_j c_k R^m \frac{m!}{2^m (\frac{m}{2}!)^2 (\frac{m}{2}+1)}, \quad m = i+j+k \,|\, m \text{ is even}} \tag{A30}$$

Which brings us back to the very familiar structure of the turbine power ~~equation~~ Equation 2.

Proving that there exists a general analytical solution for the turbine power output for any continuous function $v(h)$ as an inflow of a wind turbine.

This large fraction of factorials, is separated for readability and defined as K_m, and only has to be calculated for even values of m and can be found for $m \leq 10$ in Table A1:

$$K_m = \frac{m!}{2^m \left(\frac{m}{2}!\right)^2 \left(\frac{m}{2}+1\right)}, \quad m = i+j+k \,|\, m \text{ is even} \tag{A31}$$

Table A1. Look-up table for values of m for the large factorial fraction K_m.

m	fraction
0	1
2	$\frac{1}{4}$
4	$\frac{1}{8}$
6	$\frac{5}{64}$
8	$\frac{7}{128}$
10	$\frac{21}{512}$

A1 Verification: Units

As verification of this derivation, we can check the units of this equation:

$$P \rightarrow \left[W = N\,m\,s^{-1} = kg\,m^2\,s^{-3}\right], \tag{A1}$$

$$C_p \rightarrow [1], \tag{A2}$$

$$\rho \rightarrow \left[kg\,m^{-3}\right], \tag{A3}$$

$$R^2 \rightarrow \left[m^2\right], \tag{A4}$$

$$c_i, c_j, c_k \rightarrow \left[m^{1-i}s^{-1}\right], \left[m^{1-j}s^{-1}\right], \left[m^{1-k}s^{-1}\right], \tag{A5}$$

$$R^{i+j+k} \rightarrow \left[m^{i+j+k}\right]. \tag{A6}$$

Such that:

$$\left[kg\,m^2\,s^{-3}\right] = [1] \cdot \left[kg\,m^{-3}\right] \cdot \left[m^2\right] \cdot \left[m^{1-i}s^{-1}\right] \cdot \left[m^{1-j}s^{-1}\right] \cdot \left[m^{1-k}s^{-1}\right] \cdot \left[m^{i+j+k}\right] \tag{A7}$$

Which indeed agrees.

A2 Verification: Linear Shear

Additionally, we can verify whether this is correct by taking a linear equation for $v(z) = \overline{v} + az = c_0 + c_1 z$, such that $N = 1$. Starting from Equation 3, we insert $v(z)^3 = (c_0 + c_1 z)^3$ and expand:

$$v(z)^3 = c_0^3 + 3c_0^2 c_1 z + 3c_0 c_1^2 z^2 + c_1^3 z^3. \tag{A8}$$

Due to symmetry of the integral over $[-R, R]$, the odd terms vanish, such that only the z^0 and z^2 terms remain. Using the standard integrals over the rotor disk then yields:

$$P(v) = \frac{1}{2} C_p(v) \rho A \left(c_0^3 + 3c_0 c_1^2 R^2 \cdot \frac{1}{4} \right) = \frac{1}{2} C_p(v) \rho A \left(\overline{v}^3 + \frac{3}{4} R^2 a^2 \overline{v} \right) \tag{A9}$$

Which agrees with regular integration of this function.

A3 Verification: Linear Veer

Similarly, let us verify the veer equation ~~$v(z) = \overline{v}cos(\alpha_{max}\frac{z}{R})$. By taylor expansion :~~ $v(z) = \overline{v}\cos(\alpha_{max}\frac{z}{R})$ by Taylor expansion to the second order:

$$v(z) = \approx \overline{v} - \frac{\overline{v}\alpha_{\max}^2}{2R^2}z^2 + \mathcal{O}(h^4) = c_0 + c_2 z^2 \tag{A10}$$

with $c_0 = \overline{v}$, $c_1 = 0$, and $c_2 = \overline{v}\frac{\alpha_{\max}^2}{2R^2}$, where the ~~$h^4$~~ z^4 and higher terms are discarded.

Expanding $v(z)^3$ gives:

$$v(z)^3 = c_0^3 + 3c_0^2 c_2 z^2 + 3c_0 c_2^2 z^4 + c_2^3 z^6. \tag{A11}$$

Substituting into Equation 3 and using the known integrals for $z^m\sqrt{R^2 - z^2}$ leads to:

$$P(v) = \frac{1}{2}C_p(v)\rho A\left(c_0^3 + 3c_0^2 c_2 R^2 \cdot \frac{1}{4} + 3c_0 c_2^2 R^4 \cdot \frac{1}{8} + c_2^3 R^6 \cdot \frac{5}{64}\right) \approx \frac{1}{2}C_p(v)\rho A\overline{v}^3\left(1 - \frac{3}{8}\frac{\alpha_{\max}^2}{R^2}\right) \tag{A12}$$

Where we also discarded the R^4 and R^6 terms, which agrees again with the regular integration method.

Author contributions. **BvS**: Conceptualization, Data curation, Formal analysis, Funding acquisition, Investigation, Methodology, Software, Supervision, Validation, Visualization, Writing - original draft, and Writing - review & editing.

AB: Conceptualization, Data curation, Formal analysis, Investigation, Methodology, Software, Validation, Visualization, Writing - original draft, and Writing - review & editing.

CL: Data curation, Formal analysis, Investigation, Methodology, Software, Validation, Visualization, Writing - original draft, and Writing - review & editing.

HH: Data curation, Investigation, and Supervision.

ML: Conceptualization, Investigation, Methodology, Project administration, Funding acquisition, Resources, Supervision, Writing - review & editing.

Competing interests. The authors declare no competing interests.

Acknowledgements. This project has received funding from the European Union's Horizon 2020 research and innovation program under the Marie Skłodowska-Curie grant agreement No. 945363.

The authors would like to thank the Azienda Elettrica Ticinese (AET) for their logistical support, and as the providers of their wind turbine data for analysis in this project.

The research published in this publication was carried out with the support of the Swiss Federal Office of Energy SFOE as part of the SWEET consortium EDGE. The authors bear sole responsibility for the conclusions and results presented in this publication

References

Albers, A.: Turbulence and Shear Normalisation of Wind Turbine Power Curve, 2010.

Antoniou, I., Cleve, J., and Piperas, A.: Rotor Average wind speed for power curve performance, Tech. rep., https://pcwg.org/proceedings/2013-03-12/02-Rotor-Average-wind-speed-for-power-curve-performance-I-Antoniou-J-Cleve-A-Piperas-SWP.pdf, 2013.

Belu, R. and Koracin, D.: Effects of complex wind regimes and meteorlogical parameters on wind turbine performances, 2012 IEEE Energytech, pp. 1–6, 2012.

Bot, E.: Flow analysis with nacelle-mounted LiDAR, ECN Sint Maartensvlotbrug, The Netherlands, 2016.

Brown, K., Bortolotti, P., Branlard, E., Chetan, M., Dana, S., de Velder, N., Doubrawa, P., Hamilton, N., Ivanov, H., Jonkman, J., Kelley, C., and Zalkind, D.: One-to-one aeroservoelastic validation of operational loads and performance of a 2.8MW wind turbine model in OpenFAST, Wind Energy Science, 9, 2024.

Choukulkar, A., Pichugina, Y., Clack, C. T., Calhoun, R., Banta, R., Brewer, A., and Hardesty, M.: A new formulation for rotor equivalent wind speed for wind resource assessment and wind power forecasting, Wind Energy, 19, 1439–1452, 2016.

Clifton, A. and Wagner, R.: Accounting for the effect of turbulence on wind turbine power curves, vol. 524, p. 012109, IOP Publishing, ISBN 1742-6596, issue: 1, 2014.

Elliott, D. L. and Cadogan, J. B.: Effects of wind shear and turbulence on wind turbine power curves, Tech. rep., Pacific Northwest Lab., Richland, WA (USA), 1990.

Emeis, S.: How Well Does a Power Law Fit to a Diabatic Boundary-Layer Wind Profile?, 2005.

Gasser, J., van Schaik, B. J. A., Huwald, H., and Lehning, M.: Wind turbine performance in high-alpine terrain as influenced by temperature, snow cover and turbulence, Energy Reports, https://doi.org/10.1016/j.egyr.2026.109322, 2026.

IEC: 12-1:Power performance measurements of electricity producing wind turbines, TC 88 Wind energy generation systems, pp. 61 400–12–1:2022, 2022.

Jonkman, J.: The New Modularization Framework for the FAST Wind Turbine CAE Tool, in: 51st AIAA Aerospace Sciences Meeting including the New Horizons Forum and Aerospace Exposition, https://doi.org/10.2514/6.2013-202, _eprint: https://arc.aiaa.org/doi/pdf/10.2514/6.2013-202, 2013.

Letizia, S., Bodini, N., Brugger, P., Scholbrock, A., Hamilton, N., Porté-Agel, F., Doubrawa, P., and Moriarty, P.: Holistic scan optimization of nacelle-mounted lidars for inflow and wake characterization at the RAAW and AWAKEN field campaigns, vol. 2505, p. 012048, IOP Publishing, ISBN 1742-6596, issue: 1, 2023.

Mata, S. A., Pena Martínez, J. J., Bas Quesada, J., Palou Larrañaga, F., Yadav, N., Chawla, J. S., Sivaram, V., and Howland, M. F.: Modeling the effect of wind speed and direction shear on utility-scale wind turbine power production, Wind Energy, 27, 873–899, publisher: Wiley Online Library, 2024.

Murphy, P., Lundquist, J. K., and Fleming, P.: How wind speed shear and directional veer affect the power production of a megawatt-scale operational wind turbine, Wind Energy Science, 5, 1169–1190, https://doi.org/10.5194/wes-5-1169-2020, 2020.

Niayifar, A. and Porté-Agel, F.: A new analytical model for wind farm power prediction, vol. 625, p. 012039, IOP Publishing, ISBN 1742-6596, issue: 1, 2015.

Redfern, S., Olson, J. B., Lundquist, J. K., and Clack, C. T.: Incorporation of the rotor-equivalent wind speed into the weather research and forecasting model's wind farm parameterization, Monthly Weather Review, 147, 1029–1046, 2019.

Rettenmeier, A., Anger, J., Bischoff, O., Hofsäß, M., Schlipf, D., and Würth, I.: Nacelle-based lidar systems, Remote Sensing for Wind Energy, DTU Wind Energy-E-Report-0029 (EN), pp. 157–170, 2013.

Rosmin, N., Watson, S. J., and Tompson, M.: Power Limitation at High Wind Speeds for a Variable Speed Fixed Pitch Wind Turbine Using Closed-Loop Scalar Control, Renewable energy & power quality journal, 1, 1043–1046, 2010.

Santos, Y., Haas, P., Reinaldo, Passos, Taves, J. C., and Santa, F. F.: Effects of turbulence , wind shear , wind veer , and atmospheric stability on power performance : a case study in Brazil, 2015.

Sedaghat, A., Gaith, M. S., Khanafer, K., and Bani-Hani, E. H.: Rated wind speed reality or myth for optimization in design of wind turbines, 2016 Eleventh International Conference on Ecological Vehicles and Renewable Energies (EVER), pp. 1–4, 2016.

Sprague, M. A., Ananthan, S., Vijayakumar, G., and Robinson, M.: ExaWind: A multifidelity modeling and simulation environment for wind energy, Journal of Physics: Conference Series, 1452, 012 071, https://doi.org/10.1088/1742-6596/1452/1/012071, 2020.

Stull, R. B.: An Introduction to Boundary Layer Meteorology, Atmospheric and Oceanographic Sciences Library, 13, Springer Netherlands, Dordrecht, 1st ed. 1988. edn., ISBN 94-009-3027-5, publication Title: An Introduction to Boundary Layer Meteorology, 1988.

Troldborg, N., Andersen, S. J., Hodgson, E. L., and Forsting, A. M.: Brief communication: How does complex terrain change the power curve of a wind turbine?, Wind Energy Science Discussions, 2022, 1–8, publisher: Göttingen, Germany, 2022.

Vahidzadeh, M. and Markfort, C. D.: Modified power curves for prediction of power output of wind farms, Energies, 12, 1805, publisher: MDPI, 2019.

Vahidzadeh, M. and Markfort, C. D.: An induction curve model for prediction of power output of wind turbines in complex conditions, Energies, 13, 891, publisher: MDPI, 2020.

Van Sark, W. G., Van der Velde, H. C., Coelingh, J. P., and Bierbooms, W. A.: Do we really need rotor equivalent wind speed?, Wind Energy, 22, 745–763, 2019.

van Schaik, B., Lehning, M., and Huwald, H.: Sequential Wind-Doppler LiDAR wind profile measurements on the Gotthard pass in Switzerland - Summer 2023, https://doi.org/https://doi.org/10.5281/zenodo.14524723, 2024.

van Schaik, B., Baruzier, A., Loyer, C., Huwald, H., and Lehning, M.: A Novel Analytical Tool to Capture Wind Profile Variability for Wind Energy Assessment: Fast, Simple, and Beyond State-of-the-Art in Complex Terrain, https://doi.org/10.5281/zenodo.17804408, 2025a.

van Schaik, B., Huwald, H., and Lehning, M.: Resolving three-dimensional wind velocity fields with sequential wind-Doppler LiDAR for wind energy in the complex terrain-Gotthard Pass, Switzerland, Open Research Europe, 5, 9, publisher: F1000 Research Limited, 2025b.

van Schaik, B. J., Lehning, M., and Huwald, H.: Assessing wind dynamics and turbine power at Princess Elisabeth station, Antarctica, using Doppler wind LiDAR and vertical array anemometers, Energy Conversion and Management, 352, 121 074, https://doi.org/https://doi.org/10.1016/j.enconman.2026.121074, 2026.

van Schaik, B. J. A., Huwald, H., and Lehning, M.: Antarctic Wind Atlas: Gradient-Boosting-Based Quantile Mapping on 15 Years of Climatological Reanalysis, Bulletin of the American Meteorological Society, 107, E546 – E563, https://doi.org/10.1175/BAMS-D-25-0096.1, 2026.

Wagner, R., Antoniou, I., Pedersen, S. M., Courtney, M. S., and Jørgensen, H. E.: The influence of the wind speed profile on wind turbine performance measurements, Wind Energy: An International Journal for Progress and Applications in Wind Power Conversion Technology, 12, 348–362, 2009.

Wagner, R., Courtney, M., Gottschall, J., and Lindelöw-Marsden, P.: Accounting for the speed shear in wind turbine power performance measurement, Wind Energy, 14, 993–1004, publisher: Wiley Online Library, 2011.

Wagner, R., Cañadillas, B., Clifton, A., Feeney, S., Nygaard, N., Poodt, M., Martin, C. S., Tüxen, E., and Wagenaar, J. W.: Rotor equivalent wind speed for power curve measurement – comparative exercise for IEA Wind Annex 32, Journal of Physics: Conference Series, 524, 012 108, https://doi.org/10.1088/1742-6596/524/1/012108, 2014.